ON THE EFFECT OF STATIC AND DYNAMIC CONTACT ANGLES ON CONDENSATION HEAT TRANSFER

by

POUYA SHARBATI

Submitted to the Graduate School of Engineering and Natural Sciences

in partial fulfillment of the requirements for the degree of

Master of Science

Sabanci University

July 2023

ABSTRACT

ON THE EFFECT OF STATIC AND DYNAMIC CONTACT ANGLES ON HUMID AIR CONDENSATION HEAT TRANSFER

POUYA SHARBATI

MECHATRONICS ENGINEERING M.Sc. THESIS, JULY2023

Thesis Supervisors: Prof. Dr. Ali Koşar, Asst. Prof. Dr. Abdolali K. Sadaghiani

Keywords: Condensation, Surface modification, Static contact angle, Dynamic contact angle, Contact angle hysteresis, Droplet removal, Humid air condensation

Surface modification is a widely utilized technique for enhancing condensation heat transfer. Two main properties of surfaces in manipulation of condensation heat transfer are the contact angle and contact angle hysteresis. This study focuses on the influence of contact angle (CA) and contact angle hysteresis (CAH) on humid air condensation. For this, hydrophilic and hydrophobic surfaces with varying CA and CAH values were fabricated and tested in a humidity-controlled climate chamber at different relative humidity levels. Three hydrophilic surfaces samples with a contact angle of approximately 70° and CAH values of 10°, 20°, and 42° were tested. Two hydrophobic

surfaces with a contact angle of approximately 110° and CAH values of 21° and 42°were also prepared as well as a hydrophobic surface with a contact angle of 96° and a CAH of 43°. The role of CA and CAH in different stages of condensation cycle was investigated. Our findings show that while CA plays the main role in droplet nucleation, CAH has a significant impact on droplet coalescence and departure. Increasing CAH while keeping CA constant has a negative effect on condensation heat transfer in all wettability levels. However, the relationship between changes in CA while keeping CAH constant does not have the same trend in the condensation heat transfer performance for every case. Changing CAH for lower CAH values led to a greater impact on enhancing condensation heat transfer than higher values. Moreover, increasing CAH on hydrophobic surfaces had a more significant effect than on hydrophilic surfaces. Additionally, decreasing CAH had a more pronounced effect on improving condensation heat transfer than increasing CA. The findings emphasize on the importance of considering both the static contact angle and dynamic contact angle in the surface design to have the optimum condensation heat transfer performance.

ÖZET

YÜKSEK SICAKLIKLI Bi-2212 SÜPER İLETKEN FİLMLERİN SIVI FAZ EPİTAKSİ İLE BÜYÜMESİ VE KARAKTERİZASYONU

POUYA SHARBATI

Yüksek Lisans Tezi, Temmuz 2023

Danışman: Prof. Dr. Ali Koşar, Asst. Prof. Dr. Abdolali K. Sadaghiani

Yüzey modifikasyonu, kondensasyon ısı transferini artırmak için yaygın olarak kullanılan bir tekniktir. Kondensasyon ısı transferinin manipülasyonunda yüzeylerin iki ana özelliği temas açısı ve temas açısı histerezisidir. Bu çalışma, temas açısı (CA) ve temas açısı histerezisi (CAH)nin nemli hava kondensasyonu üzerindeki etkisine odaklanmaktadır. Bu amaçla, farklı CA ve CAH değerlerine sahip hidrofilik ve hidrofobik yüzeyler hazırlandı ve farklı bağıl nem seviyelerinde nem kontrolü yapılan bir iklim odasında test edildi. Yaklaşık olarak 70° temas açısına ve 10°, 20° ve 42° CAH değerlerine sahip üç hidrofilik yüzey örneği test edildi. Ayrıca, yaklaşık olarak 110° temas açısına ve 21° ve 42° CAH değerlerine sahip iki hidrofobik yüzey hazırlandı, ayrıca 96° temas açısına ve 43° CAH'a sahip bir hidrofobik yüzey de. CA ve CAH'ın kondensasyon döngüsünün farklı aşamalarındaki rolü araştırıldı. Bulgularımız, CA'nın damla nükleasyonunda başrol oynarken, CAH'ın damla birleşimi ve ayrılmasında önemli bir etkisi olduğunu göstermektedir. CA sabit tutulurken CAH'ı artırmak, tüm ıslanabilirlik seviyelerinde

kondensasyon ısı transferini olumsuz etkiler. Ancak CA'yı sabit tutarken CA'da meydana gelen değişikliklerin kondensasyon ısı transferi performansı için her durumda aynı trendi takip etmediği görülmüştür. Daha düşük CAH değerleri için CAH'ı değiştirmek, yüzeylerin kondensasyon ısı transferini artırmada daha büyük bir etkiye sahipti. Dahası, hidrofobik yüzeylerde CAH'ı artırmak, hidrofilik yüzeylerdekinden daha büyük bir etki yarattı. Ayrıca, CAH'ı azaltmak, CA'yı artırmaktan kondensasyon ısı transferini iyileştirmede daha belirgin bir etkiye sahipti. Bulgular, optimum kondensasyon ısı transferi performansına sahip olmak için yüzey tasarımında hem temas açısını hem de temas açısı histerezisini dikkate almanın önemini vurgulamaktadır.

Anahtar Kelimeler: Condensation, Surface modification, Static contact angle, Dynamic contact angle, Contact angle hysteresis, Droplet removal, Humid air condensation

AKNOWLEDGMENTS

I am deeply grateful to my esteemed supervisors, Prof. Dr. Ali Koşar and Asst. Prof. Dr. Abdolali K. Sadaghiani, for their unwavering support, guidance, and invaluable expertise throughout my Master's studies. I consider myself incredibly fortunate to have had the opportunity to learn from them and be their student.

I would also like to thank the distinguished members of my jury: Prof. Dr. Metin Muradoğlu from Koc University, Assoc. Prof. Dr. Emre Erdem from Sabanci University, and Assoc. Prof. Dr. Yegân Erdem from Bilkent University, for their valuable input and insightful comments.

Furthermore, I want to express my deepest gratitude to my dear family, especially my beloved wife, Ara, for her unwavering support and dedicated presence throughout this remarkable journey. I am truly fortunate to have her by my side.

Table of Contents

List of Figures

List of Tables

1. INTRODUCTION

Condensation is a crucial phase change phenomenon in the nature and industrial applications. It occurs when a solid surface comes into contact with moist air or vapor, while the temperature of the surface is maintained below the saturation temperature. During condensation, the vapor phase transforms into the liquid phase, forming a condensed layer on the surface. Condensation heat transfer enhancement plays a vital role in reducing the energy consumption and costs in related industries. Some emerging applications include water harvesting [1,2] desalination [3,4], electronic thermal management systems [5], electronics cooling [6], power generation systems [7], and heat exchangers [8]. Improving condensation heat transfer leads to high heat transfer coefficients (HTC) and enhanced process efficiency in each application.

The condensation mode depends on the operating circumstances, thermo-physical parameters of the condensate, and surface characteristics [9]. The surface condition significantly influences the pace and condensation mode [10]. Therefore, proper surface modification could increase energy efficiency without changing operating conditions. The wettability of a surface indicates whether a liquid spreads over the surface area or whether it stays in a spherical shape on the surface. Water loses its drop form and spreads over the surface on wetting surfaces, while on a non-wetting surface, water keeps its spherical shape. According to the degree of wettability of surfaces, they can be classified into four distinct groups: super-hydrophilic and hydrophilic ones, which are considered as wetting surfaces, and hydrophobic and super-hydrophobic ones, which are considered as non-wetting surfaces (**Figure 1.1**).

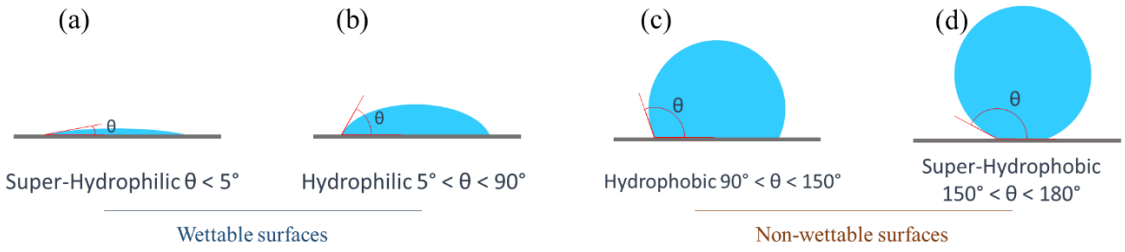

Figure 1.1 Classification of surfaces based on water droplet contact angle. (a) Super-Hydrophilic surface, (b) Hydrophilic surface, (c) Hydrophobic, (d) Super-Hydrophobic. (a) and (b) are wettable surfaces, while (c) and (d) are non-wettable surfaces.

Depending on its mode, condensation can be classified into filmwise (FWC) and dropwise (DWC) condensation [10]. Over the past century, research findings have shown that heat transfer rates during steam dropwise condensation on non-wetting surfaces can be 10 times higher than filmwise condensation on wetting substrates [11–13]. In FWC, the condensate forms a thin film on the surface, and liquid film introduces a thermal resistance to the heat transfer process, thereby deteriorating heat transfer. While the droplets remain partially spherical and slide down in DWC when they reach a critical diameter (when the gravitational/shear forces equal adhesion force), they clear the surface and allow vapor to enter and condense. The absence of a liquid film reduces the thermal resistance, increases the available surface area for vapor condensation, and ultimately enhances heat transfer [14].

Numerous studies have employed various fabrication methods to achieve hydrophobicity and super-hydrophobicity on surfaces [15,16], promoting dropwise condensation and achieving more efficient heat transfer during condensation processes. In a related study by Chehrghani et al. [17], superhydrophobic and hydrophobic surfaces were fabricated on a copper substrate. They investigated the performance of surfaces in flow condensation at various steam mass fluxes and different inlet vapor qualities. The results demonstrated that the combination of increased mass flux and water-repellent properties of the nanostructured superhydrophobic surface led to an enhancement in flow condensation heat transfer compared to a bare copper surface. In another experimental study, Thomas et al. [18] tested three hierarchical superhydrophobic surfaces with low contact angle hysteresis. These surfaces exhibited similar macroscopic wettability and average roughness but were coated with three different nanocoating hydrophobic agents. Their investigation aimed to examine the effect of these nanocoatings on humid air condensation. The Glaco-coated hierarchical surface, which exhibited a self-propelled jumping mechanism, was found to have a lower condensation rate. Based on their findings, they concluded that the self-propelled jumping mechanism observed on the Glaco-coated surface was not suitable for atmospheric water harvesting applications, despite the positive results reported in other studies regarding the enhancement of heat transfer performance through coalescence-induced droplet jumping [19,20].

Superhydrophobic surfaces have been considered as a promising approach to enhance drainage during condensation. However, the condensation theory [21] suggests that the nucleation rate of phase change is inversely proportional to the surface contact angle. This creates a challenge where improved drainage competes with drop formation and growth. To address this issue, recent studies have explored patterned condensation surfaces with different wettabilities [21–23]. These studies have shown that such surfaces could enhance condensation rates, which were not explained by the traditional nucleation theory [24]. Daniel et al. [25] demonstrated that droplets exhibit random movement from low-wettability regions to regions with higher wettability. Oestreich et al. [26] observed that a hybrid surface with a constructal-like pattern (combining superhydrophobic and hydrophilic properties) had improved heat transfer compared to pure superhydrophobic or hydrophilic surfaces.

Most of the related studies have focused only on how to maintain DWC by utilizing non-wetting surfaces. However, as long as the drainage of the condensate droplets from the surface is not performed efficiently, the improvement of the heat transfer performance

will be limited [27]. While the surface wettability has been extensively investigated regarding condensation heat transfer [28], another critical surface property with the potential of having a significant impact on condensation heat transfer is the contact angle hysteresis (CAH) [29–31]. However, relatively few studies have focused on the influence of contact angle hysteresis on condensation heat transfer. Contact angle hysteresis occurs when the advancing and receding contact angles differ, which can be caused by surface irregularities or chemical heterogeneities. It physically represents the dissipated energy involving the droplet's movement along the solid surface. In a related study, Cha et al. [32] challenged the notion that dropwise condensation is limited to non-wetting surfaces. Their findings suggest that DWC can occur on any surface, and the ability to sustain stable dropwise condensation is primarily determined by the contact angle hysteresis rather than the surface wettability. The mobility of droplets on both homogeneous and heterogeneous surfaces is mainly governed by CAH, highlighting its importance in achieving DWC. While previous research focused on hydrophobic surfaces, the authors proposed the possibility of achieving stable DWC on solid hydrophilic surfaces with low CAH. Although there are studies that indicate the positive effect of CAH on the condensation performance [27,33], there is not any study directly comparing the effect of contact angle and contact angle hysteresis to each other. To address the gap of knowledge in the literature, we fabricated a set of surfaces to investigate the impact of contact angle (CA) and contact angle hysteresis (CAH) on condensation heat transfer. Three hydrophilic surfaces were prepared, each with a contact angle of ~70° and varying CAH values of 10°, 20°, and 42°. Additionally, two hydrophobic surfaces with a contact angle of ~110° and CAH values of 21° and 42° and one with a contact angle of 96° and CAH of 43° were fabricated. The fabricated surfaces were subjected to testing in a humidity-controlled climate chamber at 80%, 90%, and 100% relative humidity levels. The obtained results highlight the complex interplay among CA, CAH, and condensation heat transfer, emphasizing on the need for careful consideration of both parameters in the surface design for an enhanced condensation heat transfer performance.

2. METHODOLOGY

2.1. Surface Fabrication and Characterization

2.1.1. Hydrophilic Surfaces

Smooth silicon wafers (P type, ⟨100⟩ orientation, 0 to 100 Ω·cm, single side polished) were used as the base substrate. Silicon wafers were diced into 2 × 2 cm^2 samples. Diced silicon substrates were first cleaned in an ultrasonic bath of acetone and thereafter ethanol for 10 minutes, followed by drying with nitrogen. The bare silicon wafer after cleaning was used as hydrophilic surface number 1 (S_{Phil1}).

The contact angle (CA) and contact angle hysteresis (CAH) of the cleaned surfaces would naturally change over time due to factors such as oxidation from exposure to oxygen and moisture and the absorption of organic particles. [34] A cleaned surface of eight days of ambient exposure in the lab was used as the hydrophilic surface number 2 (S_{Phil2}).

Another cleaned sample was used for condensation tests for three days, 1-hour test each day, then dried using nitrogen and exposed to the ambient environment for ten days. The extended exposure combined with the residuals from the tests led to an increase in CAH. This sample was designated as the hydrophilic surface number 3 (S_{Phil3}).

2.1.2 Hydrophobic Surfaces

To fabricate hydrophobic surface number 1 (S_{Phob1}), the diced silicon wafers were washed with Acetone, Isopropanol and DI water, followed by blowing N_2 gas to eliminate any remaining contaminants. Subsequently, a thin layer of octafluorocyclobutane (C_4F_8) was coated on the surfaces through chemical vapor deposition Oxford DRIE machine (Oxford PlasmaLab System 100 ICP 300 Deep RIE) to functionalize the surfaces to have hydrophobic behavior. The deposition process involved specific parameters, including a pressure of 30 mTorr, RF power of 5 Watts, ICP power of 1500 Watts, and a deposition temperature of 5°C. The plasma polymerization was carried out continuously under the CW mode.

Hydrophobic surface number 2 (S_{Phob2}) was prepared using spin coating a thin layer (<10µm) of PDMS (Polydimethylsiloxane) on the surface. The diced wafers were washed with Acetone, Isopropanol, and DI water, followed by blowing N_2 gas. The PDMS and curing agent were mixed in a mass ratio of 10:1. The mixed PDMS solution was poured on the sample and spin-coated at 3500 rpm for 4 minutes. Following the spin coating process, the PDMS layer was cured by placing the sample on a hot plate set to a temperature of 115°C for 3 hours. This curing step ensured the solidification and stability of the PDMS layer on the surface.

To fabricate hydrophobic surface number 3 (S_{Phob3}), the S_{Phob1} sample was subjected to additional treatment in an oxygen plasma cleaner device. The purpose of this treatment was to modify the surface properties of the sample. The oxygen plasma exposure had the effect of reducing the hydrophobicity of the surface. The sample was subjected to 30 seconds of oxygen plasma treatment using the Harrick Plasma cleaner device at a pressure of 400 mTorr and an oxygen flow rate of 20 sccm.

2.2.Characterization

Water contact angle measurements and contact angle hysteresis measurements techniques were made to characterize the surfaces. The contact angles were measured using an Attension® Theta Lite optical tensiometer. For each surface, 5µL water droplets were

carefully placed at multiple locations. Six sessile contact angle measurements were conducted on each surface, and the average values were obtained. The advancing and receding contact angles were determined by inflating and deflating a sessile drop. This measurement was repeated at six different points on each surface, and the average values were calculated. The static, advancing, and receding contact angles of the surfaces are presented in **Table 2.1** and **Figure 2.1**. **Figure 2.2** illustrates techniques for measuring contact angles of water droplets on the samples.

It is important to note that the CA and CAH of the surfaces were measured before and after each test. The CA of the surfaces varied by up to 2 degrees, while the advancing and receding angles changed by up to 1 degree and 3 degrees, respectively. In order to maintain result consistency, new surfaces were fabricated for each test.

Table 2.1 Properties of the tested samples

Sample name	***CA (θ_E)***	***ACA (θ_A)***	***RCA(θ_R)***	***CAH ($\Delta\theta=\theta_A-\theta_R$)***
S_{Phil1}	68±1	70±1	60±1	10
S_{Phil2}	70±1	76±1	56±2	20
S_{Phil3}	70±2	82±2	40±2	42
S_{Phob1}	112±2	122±1	102±1	21
S_{Phob2}	112±1	128±1	86±2	42
S_{Phob3}	96±2	108±2	65±1	43

CA: Young's Contact Angle, ACA: Advancing Contact Angle, RCA: Receding Contact Angle, CAH: Contact Angle Hysteresis

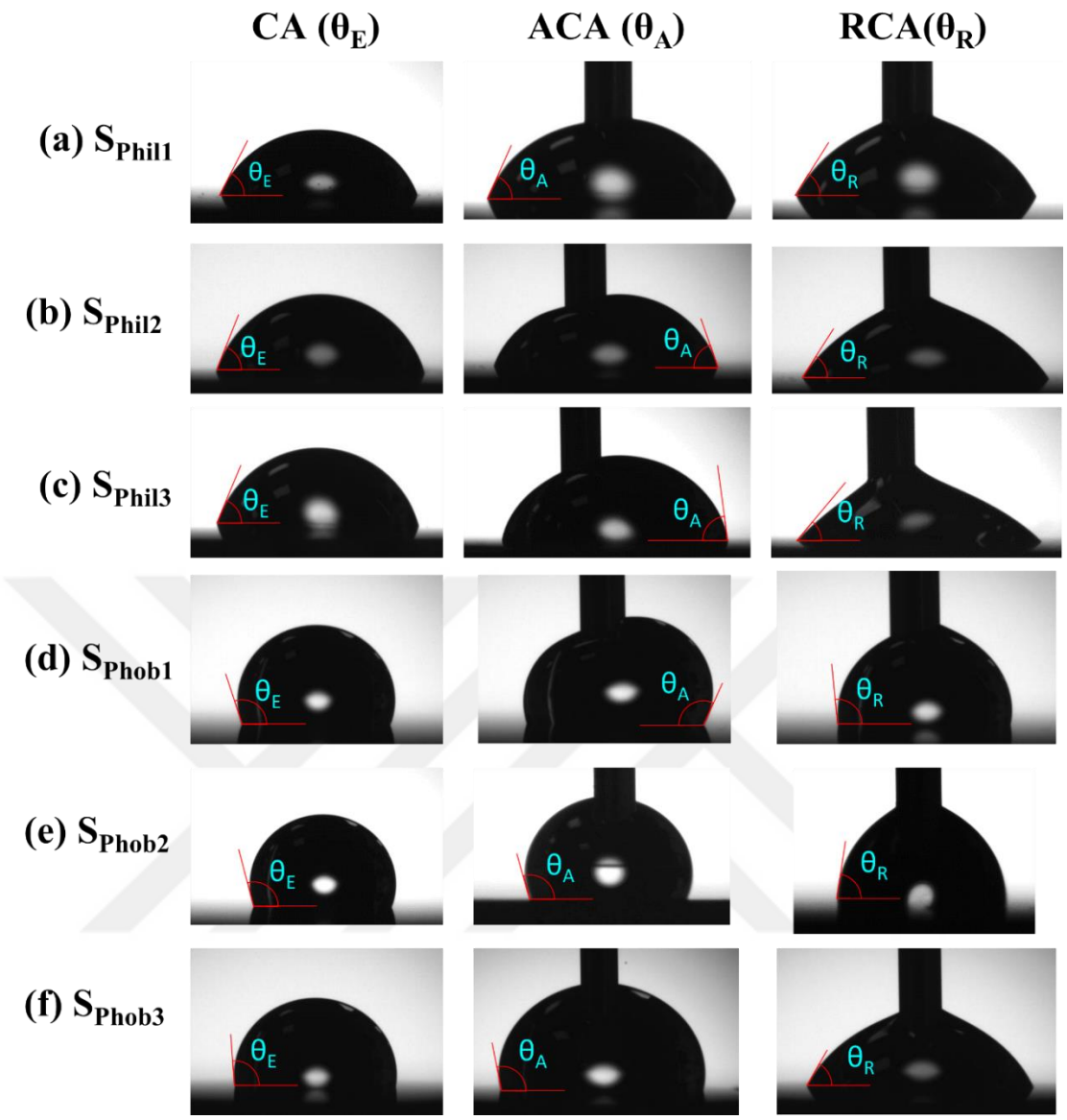

Figure 2.1 Static, advancing, and receding contact angles of water droplet on different surfaces.

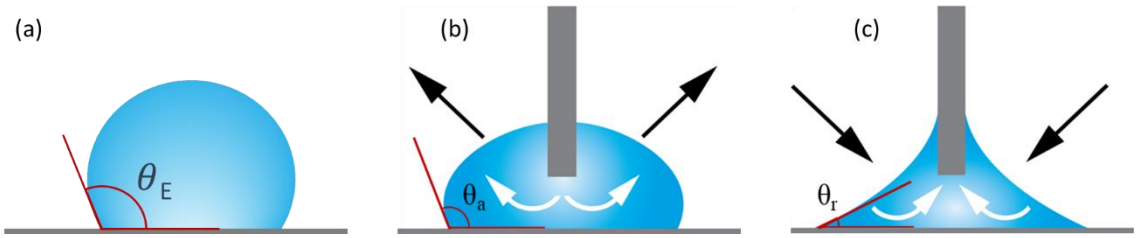

Figure 2.2 Demonstration of techniques for measuring contact angles of water droplets on the samples. (a) using a sessile droplet to measure static contact angle, (b) Inflating a droplet until its contact line starts to expand to measure advancing contact angle, (c) Deflating a droplet until its contact line starts to expand to measure receding contact angle.

2.3. Experimental Setup and Procedure

The effect of static and dynamic contact angles on humid air condensation was investigated by conducting experiments at three different relative humidity levels: 80%, 90%, and 100%. The experiments were conducted in a controlled environment using a climate chamber to minimize external influences. A constant room temperature of 21.5°C was maintained throughout the experiments. By maintaining specific relative humidity levels, accurate observations and analysis of the condensation process were possible, providing insights into the role of CA and CAH in humid air condensation.

To ensure accurate measurements and minimize wall effects, the test section was positioned in the middle of the chamber during the experiments. **Figure 2.2** illustrates the experimental setup employed in the study. The sample was vertically mounted on a Peltier device using thermally conductive paste (**Figure 2.2 b**). The Peltier device was connected to a water circulator block (**Figure 2.2 b**), with a chiller supplying cold water at 5°C to the circulation unit to enable the Peltier device to maintain lower temperatures. Subcooling of the sample surface was maintained by setting the Peltier temperature to 1°C. Surface temperature monitoring was carried out using a T-type thermocouple, and continuous temperature measurements were recorded using an external data logger. To maintain measurement precision, the thermocouple data was compared with thermal camera measurements prior to each test.

In the chamber, humidity was generated using a commercial humidifier, and real-time humidity and temperature monitoring was conducted using two thermo-hygrometers positioned at different locations within the chamber. It is important to note that the reported temperature for the climate-controlled chamber represents the instantaneous average of the probe readings. A series of tests were performed to determine the optimal voltage and current to be applied to the Peltier device to have the desired temperature and humidity levels. Once the desired conditions were reached, minimal intervention was needed to sustain the temperature and humidity, and the humidifier's dimmer was used to set humidity pulses within acceptable ranges.

Condensate water resulting from the experiments was collected in a glass vial with a diameter of 2cm and was placed beneath the sample surface. To account for experimental uncertainties and variability in process variables, the experiments were repeated for multiple times using different samples, each run lasting two hours. The presented results in this study represent the average values obtained from at least two measurements. The condensation experiments were visualized using a camera (CANON PowerShot SX60 HS) with a 10x optical zoom.

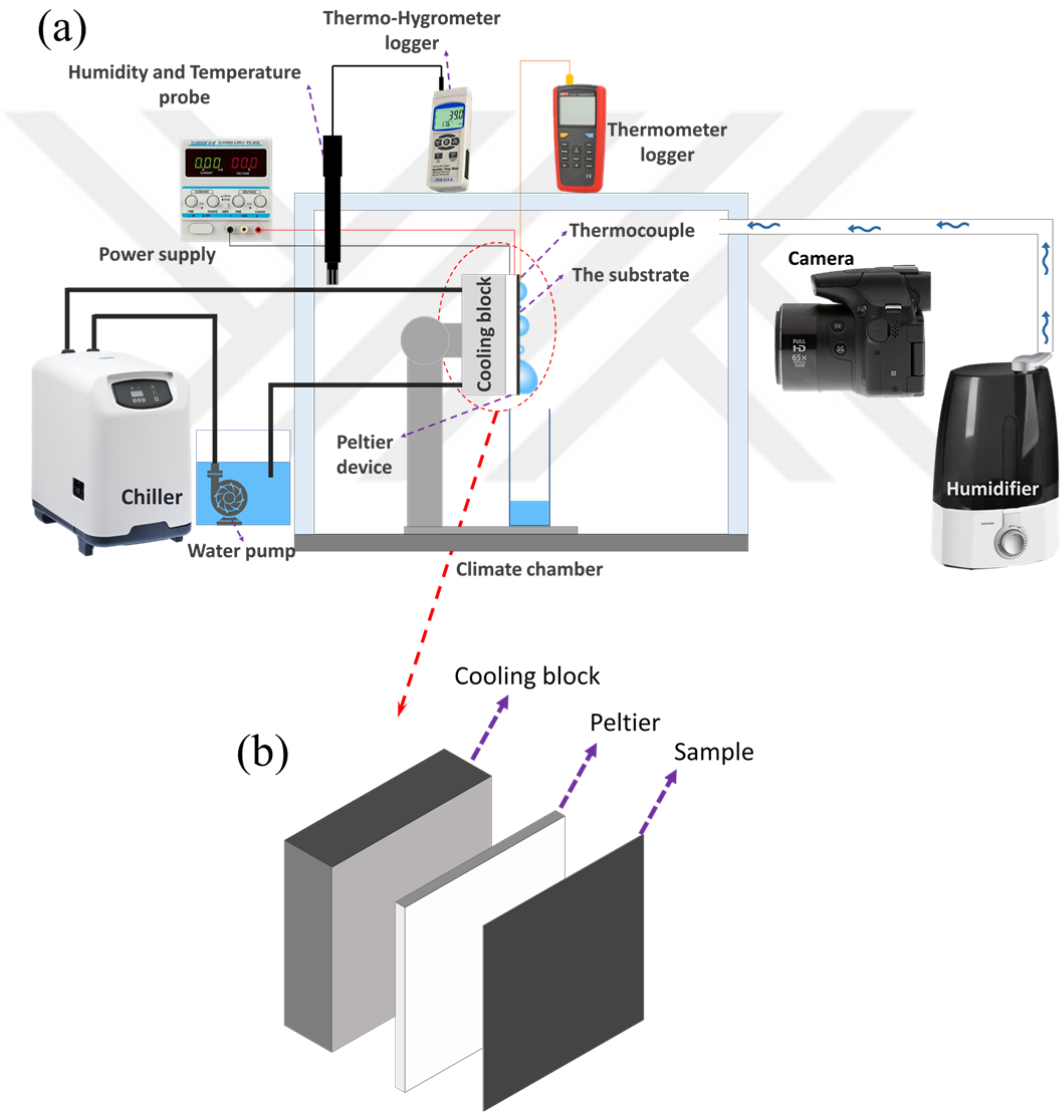

Figure 2.3 (a) Experimental setup, (b) Different parts of the test section

2.4.Image Analysis

ImageJ software, along with an in-house MATLAB code, was employed to analyze the obtained images. Frames were captured at 5-minute intervals to capture the dynamic evolution of the droplets. The analysis involved preprocessing frames for better visibility, followed by droplet detection, counting, and size measurement during the condensation process. To obtain consistent results, each experiment was repeated at least twice, and the frames from all experiments were collected, and the obtained values were averaged to reduce the error associated with the image processing method.

2.5. Data Reduction and Uncertainty Analysis

Accurately measuring the heat transfer coefficient (HTC) during condensation in humid air is challenging compared to a pure steam environment. In humid air the heat flux (q″) transferred to a cooling system from the condensing surface is relatively low [26]. Conventional techniques struggle to estimate such low heat fluxes due to the temperature difference being close to the range of thermocouple accuracy [35]. An alternative approach involves calculating the average condensation heat transfer coefficient (h) based on the amount of condensate water from the surface [36]. This method provides an estimation of HTC under humid air conditions:

$$h = \frac{\dot{m} h_{lv}}{T_{dew} - T_s} \tag{2.1}$$

The condensation rate represents the amount of water collected per unit area and unit time ($\dot{m}$) (g m^{-2} s^{-1}). It is influenced by parameters such as the latent heat during condensation (h_{lv}), dewpoint temperature (T_{dew}), and surface temperature (T_s). **Equation 1** focuses on the condensation process and does not consider other parameters such as the sensible heat transfer, heat loss by evaporation, or latent heat energy carried by the condensate remaining on the surface.

2.5.1. Uncertainty Analysis

The uncertainties in experimental parameters were evaluated by utilizing the spreadsheets provided by the device manufacturers. The uncertainties in the measured parameters are tabulated in **Table 2.2**.

Table 2.2. Measured parameters and uncertainties

Measured Parameters	Uncertainties
Weight of collected water [g]	10^{-4}
Surface temperature [K]	0.15
Relative humidity	3%
Humid air temperature [K]	0.8
Sample dimension [mm]	0.2

Applying the uncertainty propagation methodology [37], the average uncertainty in the average heat transfer coefficient is found to be ±4.2%.

2.6. Validation

In order to validate our experimental setup and methodology, we made a comparison with the results of study by Jing et al. [38]. A bare silicon sample (2×2 cm^2) was used, and the moist outlet was positioned in front of the surface at a distance of 5cm from the surface, similar to their setup. Since there was no cooling for the surfaces, we turned off our cooling devices as well. The validation test was conducted for multiple times, with varying durations (two trials for 30 minutes, two trials for 1 hour, two trials for 2 hours, and one trial for 4 hours), and the collected water was compared with the results reported by Jing et al. [38]. As depicted in **Figure 2.3**, our findings demonstrate a strong agreement

with the results presented in the study of Jing et al. [38], providing further validation for our experimental setup.

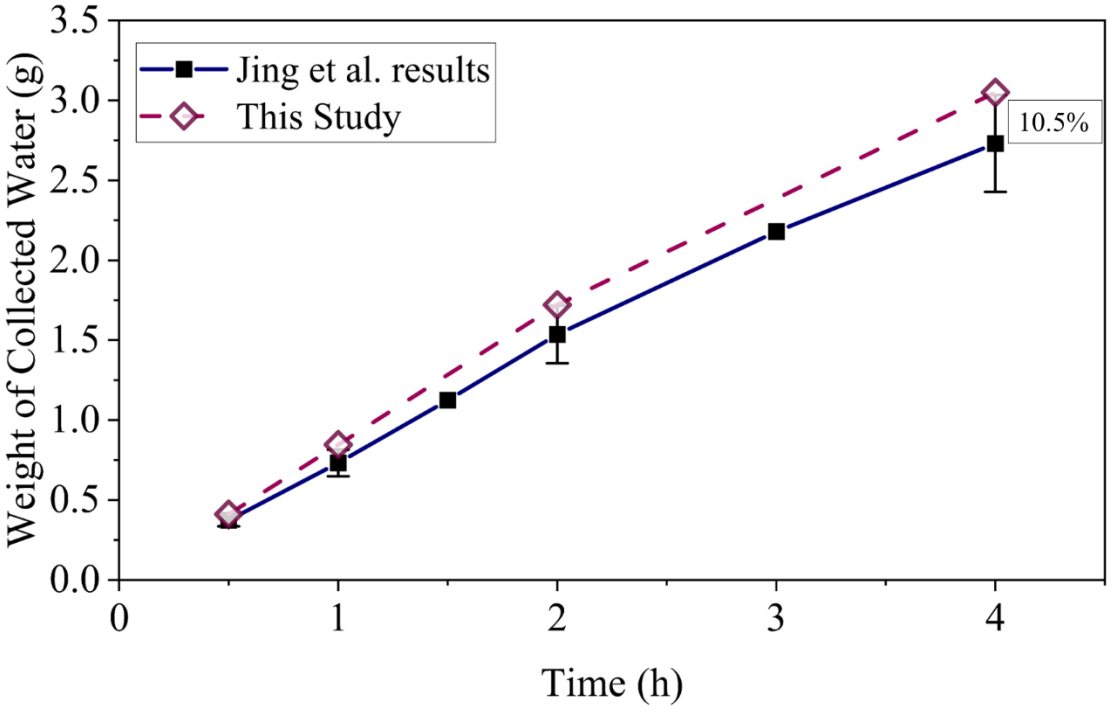

Figure 2.4 Weight of collected condensed water on the bare silicon surface: Jing et al. [38]study and this study

3. RESULT AND DISCUSSION

3.1.Visualization Study

3.1.1 Droplet Dynamics

The condensation cycle, defined as the sequence of droplet nucleation, growth, coalescence, and departure, is useful for characterizing the condensation phenomenon [11]. Condensation cycles consisting of nucleation (Stage I), growth (Stage II), coalescence (Stage III), and departure (Stage IV) are illustrated in **Figure 3.1**. In the analysis, the symbol τ represents the duration of a complete cycle. Each cycle begins as the previous cycle ends, which is indicated by the departure of large droplets from the surface. In this study, the completion of a cycle was defined as the instance when the first droplet detached from the surface. During Stage I, droplet nucleation begins. The rate at which droplets form depends on various parameters such as the surface wettability, temperature, hydrothermal properties of the vapor, and presence of non-condensable gases. To specifically study the impact of surface properties on condensation, all these parameters except the surface wettability were kept constant during the experiments. In Stage II, the droplets start to grow as vapor continuously condenses onto them. In Stage III, the droplets merge together, forming larger droplets. Eventually, when the droplets reach their maximum size, they sweep away from the surface by the gravitational force. Following the removal of the droplets, a new cycle initiates in the vacant space.

The impact of the static contact angle and contact angle hysteresis on the droplet size and shape is shown in **Figure 3.2**, indicating the four stages on S_{Phil1}, S_{Phil2}, S_{Phil3}, S_{Phob1}, S_{Phob2}, and S_{Phob3}. **Figures 3.2 d** and **e** illustrate a complete cycle of dropwise condensation observed on hydrophobic surfaces with varying CAH (S_{Phob1} & S_{Phob2}, **Table 2.1**) under the experimental conditions described earlier. As both surfaces have the same level of wettability, droplet nucleation and growth processes appear similar on these surfaces during the initial stages. However, notable differences in the droplet size and shape in Stage III arise. On S_{Phob1}, the droplets exhibit a perfectly circular geometry, and the size of the larger droplets is smaller compared to those observed on S_{Phob2}. Conversely, the droplets on S_{Phob2} have elliptical and semicircular shapes, spreading across the surface and covering a larger percentage of the area. This extended spreading increases the thermal resistance, thereby adversely affecting the heat transfer performance.

The full cycle of dropwise condensation under the same experimental conditions is shown in **Figures 3.2 b** and **c** for S_{Phil2} and S_{Phil3}, which are hydrophilic surfaces with different CAH but the same CA (**Table 2.1**). Similar to the hydrophobic surface, small droplets start to nucleate at t=0. The droplet size distribution at $\tau/5$ indicates that the droplets tend to coalesce quicker on the hydrophilic surfaces than on the hydrophobic surfaces, leading to larger droplets within a shorter period. The difference in CAH also shows itself in the droplet size and shape on hydrophilic surfaces after droplet coalescence.

S_{Phil2}, which has lower CAH, provides more uniform droplet size distribution and circularity (Frame 4 of **Figure 3.2 b**, green rectangle), while droplets on S_{Phil3}, which has higher CAH, have non-circular shapes and larger sizes (Frame 4 of **Figure 3.2 c**, pink rectangle). By comparing the hydrophobic and hydrophilic surfaces with the same CAH, it can be seen that the droplets on the hydrophilic surfaces are generally larger. The hydrophilic surfaces have higher surface energy, and water droplets spread on the surfaces. In contrast, on hydrophobic surfaces, the droplets tend to have a smaller contact line with the surface.

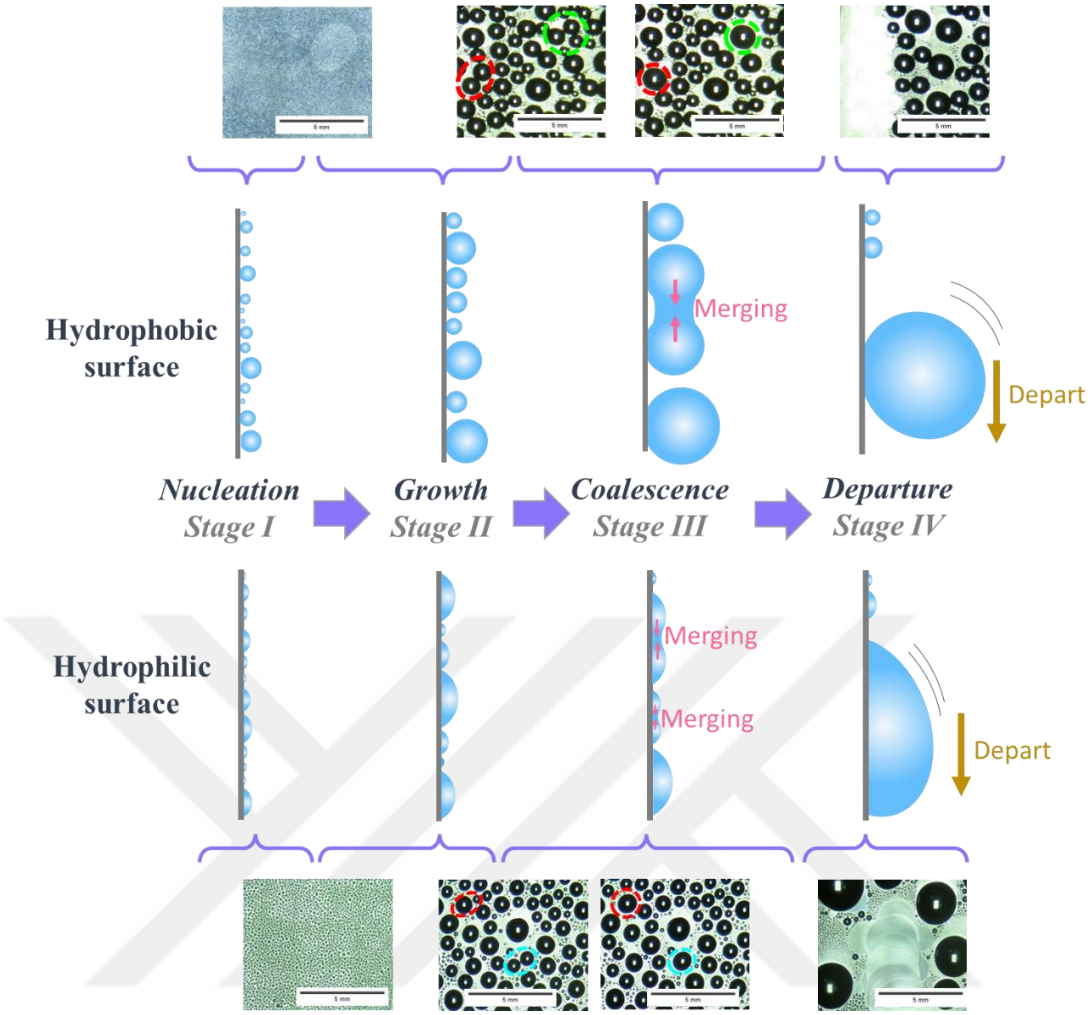

Figure 3.1 Schematic of condensation stages.

The maximum radius of droplets is affected by both the contact angle (CA) and contact angle hysteresis (CAH). As seen in **Figure 3.3**, increasing the CA decreases the maximum droplet radius. This is because droplets on hydrophilic surfaces tend to spread out due to the higher surface energy. On the other hand, droplets on hydrophobic surfaces tend to maintain a spherical shape with a smaller contact line on the surface. Additionally, increasing the CAH leads to a larger maximum droplet radius for both hydrophilic and hydrophobic surfaces (**Figure 3.3**). This is because a surface with higher CAH creates more resistance against the movement of the droplet contact line. As a result, droplets need to enlarge to overcome the surface adhesion force and to depart.

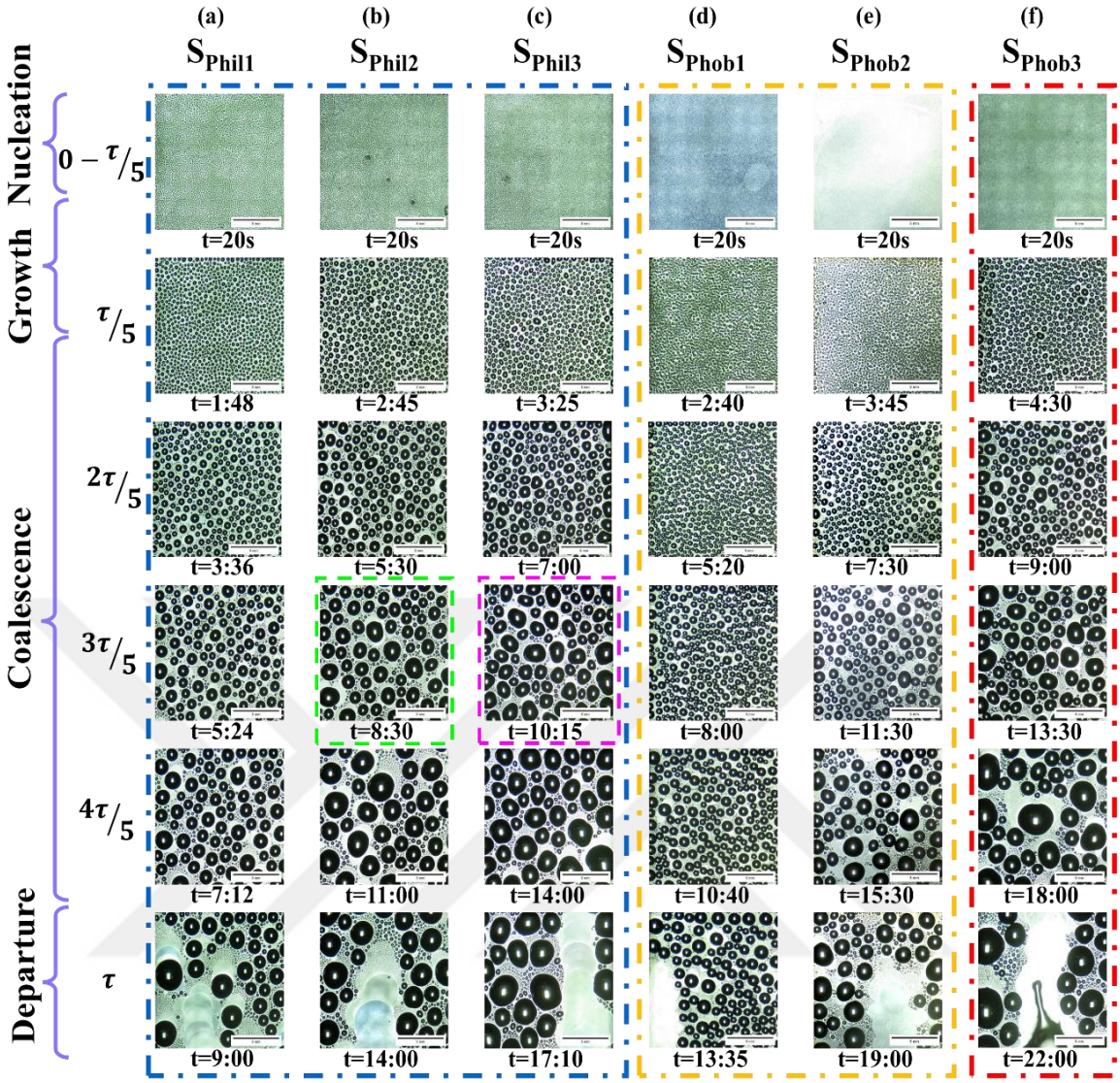

Figure 3.2 Condensation stages on (a) hydrophilic surface number 1, (b) hydrophilic surface number 2, (c) hydrophilic surface number 3, (d) hydrophobic surface number 1, (e) hydrophobic surface number 2, (f) hydrophobic surface number 3. The blue rectangle indicates hydrophilic surfaces. The yellow rectangle indicates hydrophobic surfaces with CA=112°. The red rectangle indicates the hydrophobic surface with CA=96°.

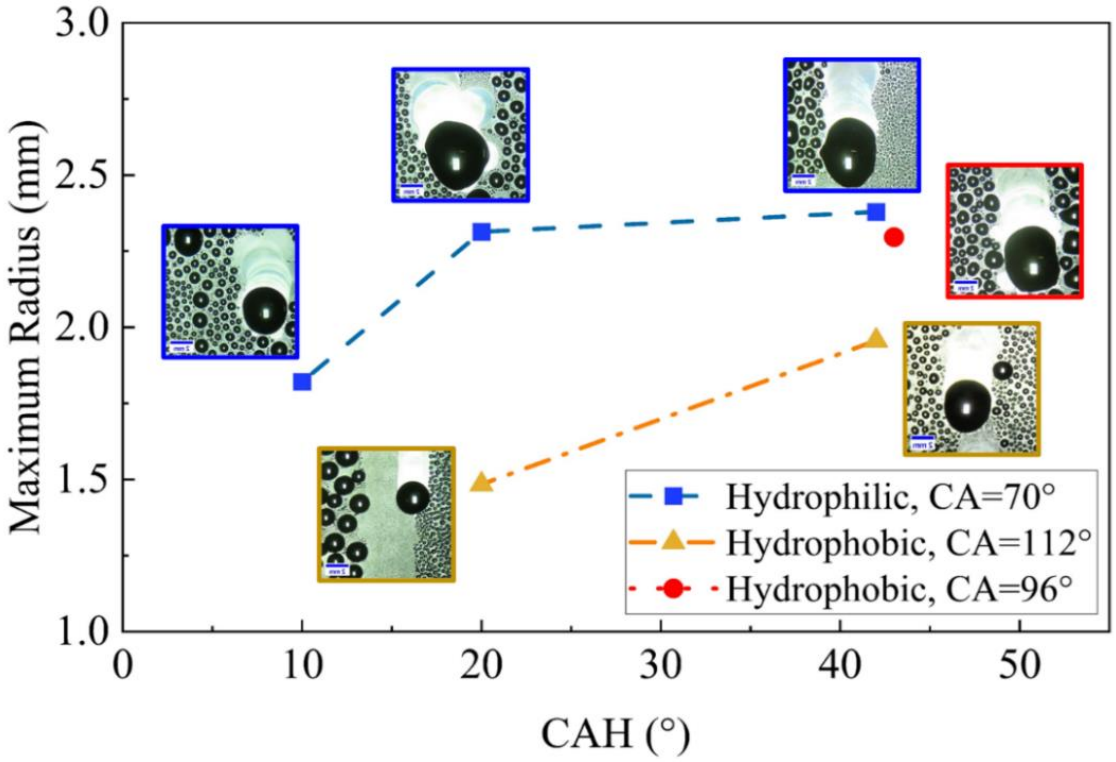

Figure 3.3 Maximum droplet radius on each surface over CAH

Figure 3.4 presents the relationship between cycle duration (τ) and CAH for hydrophilic and hydrophobic surfaces. Increasing the CAH leads to longer cycle durations for both surfaces. This can be attributed to the increased adhesion values, at which the droplets need to grow bigger to overcome the adhesion and prolong the cycle duration. Additionally, surfaces with higher CAH have larger droplet sizes (**Figure 3.3**), which results in greater surface coverage and fewer available nucleation sites. As a result, it takes longer for the droplets on surfaces with higher CAH take to reach their maximum radius and detach from the surface.

Figure 3.4 demonstrates an interesting trend regarding the effect of CAH on cycle duration (τ). Although the CAH difference between S_{Phil2} and S_{Phil3} is close to the CAH difference between S_{Phob1} and S_{Phob2}, increasing CAH has a more significant impact on τ for the hydrophobic surface (5.5 min increase in cycle duration) compared to the hydrophilic surface (3 min increase in cycle duration). This difference is linked to the inherent advantages of hydrophobic surfaces such as a larger nucleation area due to a larger r_{max} and improved droplet removal. However, when CAH increases, it adversely affects both of these advantages. Consequently, the condensation performance of

hydrophobic surfaces is more significantly influenced by increasing CAH compared to hydrophilic surfaces.

Figure 3.4 provides insight into the impact of maintaining a dynamic constant CAH while varying the static contact angle on the cycle duration (τ). For instance, when considering S_{Phob1} ($\tau_{S_{Phob1}}$=13.5 minutes) and S_{Phil2} ($\tau_{S_{Phil2}}$=14 minutes) (nearly equal CAH, **Table 2.1**), S_{Phob1}, which has a higher CA, has a slightly shorter cycle duration. Similarly, when considering S_{Phil2} ($\tau_{S_{Phil2}}$=14 minutes) and S_{Phob3} ($\tau_{S_{Phob3}}$=22 minutes) (similar CAH, **Table 2.1**), S_{Phob2}, with a higher CA, has a shorter condensation cycle duration compared to S_{Phob3}. However, an intriguing observation is seen for S_{Phil3} ($\tau_{S_{Phil3}}$=17 minutes), which has a lower CA than S_{Phob2} and S_{Phob3}, yet its cycle duration is shorter than both hydrophobic surfaces. This is due to the advantage of better droplet nucleation on S_{Phil3}, which compensates for its lower contact angle. Although hydrophobic surfaces are expected to have better droplet removal, the high CAH reduces this ability, resulting in a slower removal of droplets on S_{Phob2} and S_{Phob3}. The enhanced droplet nucleation on S_{Phil3} leads to coalescence of more droplets and faster attainment of r_{max}, which contributes to its shorter cycle duration. These findings highlight the complex interplay among CA, CAH, and condensation dynamics. They also prove that increasing the static contact angle while maintaining a constant CAH does not always follow a monotonic trend in cycle duration.

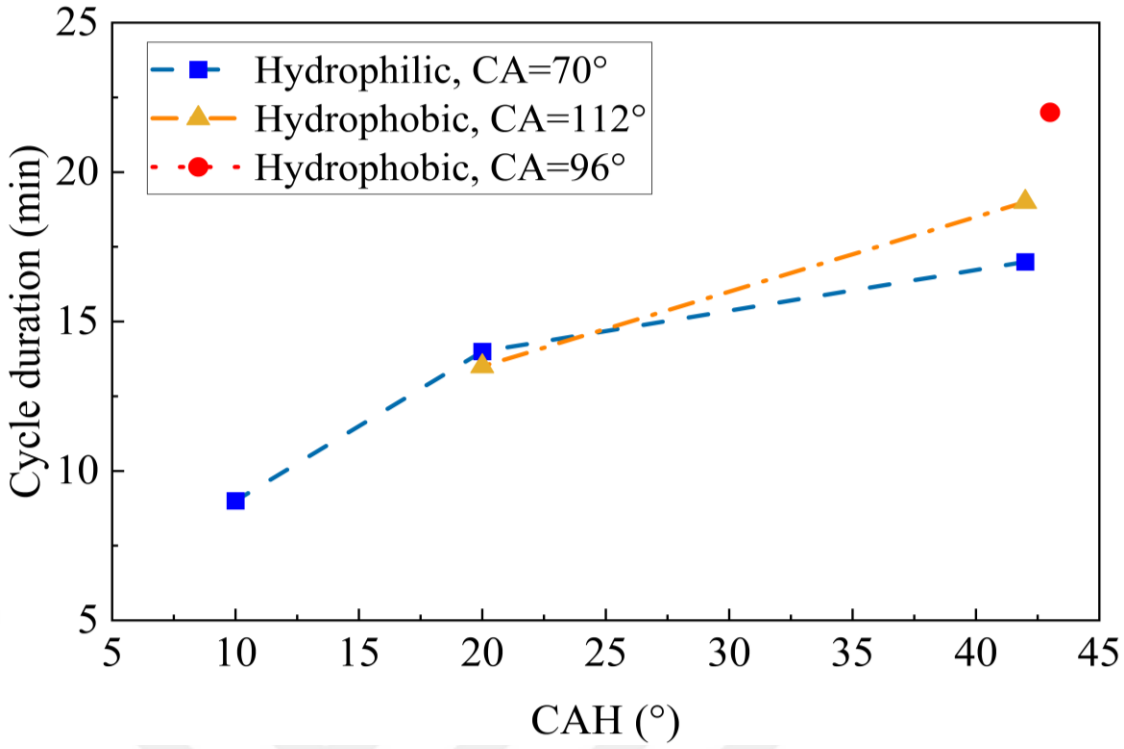

Figure 3.4 Condensation cycle durations as a function of CAH

3.1.2 Coalescence Dynamics

The behavior of droplet coalescence during condensation was observed on the tested surfaces. Surfaces with the same static contact angle but different contact angle hysteresis exhibit a similar performance in the nucleation and initial growth of droplets due to vapor condensation (**Figure 3.2**). However, the impact of CAH becomes evident in the coalescence and departure stages. **Figure 3.3** and **Figure 3.4** illustrate that increasing CAH results in a larger departure radius and longer cycle duration for both hydrophilic and hydrophobic surfaces. **Figure 3.5** provides images of droplet coalescence on the six tested surfaces. On S_{phil1}, although it is a hydrophilic surface, droplets grow uniformly, and the droplets end up with circular shape after coalescence due to the low CAH. On S_{Phil2}, as shown in the highlighted area of **Figures 3.5 c, d, and e**, droplets undergo coalescence and have non-circular and elliptical shapes due to the surface resistance to the droplets contact line movement that prevents a circular shape. Despite the higher resistance on S_{Phil2} compared to S_{Phil1}, the triple-phase line of the droplets does not completely pin to the surface. However, the movement of the triple-phase line is

significantly slower, taking approximately 12 seconds to achieve to its final state. The red mark in **Figure 3.5 l** represents the final shape of the droplet after 12 seconds of coalescence, and the green mark shows the shape right after the coalescence. This delay in relaxation adversely affects condensation heat transfer, as it postpones the nucleation of new droplets.

On S_{Phil3}, the higher contact angle hysteresis on this surface leads to increased resistance to droplet movement, which results in the pinned contact line to the surface. This can be observed in **Figures 3.5 f and g**, where three droplets are shown before and after coalescence. In the second frame, the coalesced droplet exhibits a triangular shape, which illustrates the limited shrinkage of the coalesced droplet due to the high CAH and results in the immobilization of the contact line. The irregularity in shape and non-uniformity of droplets on this surface is because of the high resistance of surface to contact line movement.

On surface S_{Phob1}, the droplet distribution is uniform and the droplets have a perfect spherical shape. Although this surface has a higher CAH compared to S_{Phil1} and has the same CAH as S_{Phil2}, two factors contribute to the ease and effectiveness of droplet coalescence for this surface. First of all, the higher CA of droplets leads to a smaller contact line and reduces the resistance force to the three-phase line movement during coalescence, which facilitates merging between droplets. Also, the higher CA results in a larger amount of residual energy and aids in the coalescence process. It is worth mentioning that coalescence events are less frequent on S_{Phob1} compared to S_{Phil1} due to its lower wettability. This lower wettability leads to fewer droplet nucleation events, resulting in a limited number of available droplets for coalescence.

S_{Phob2} and S_{Phob3} have close CAH values to S_{Phil3}, but their CA are larger. This difference in contact angle results in a greater amount of residual energy, which is an advantage for the coalescence process. On S_{Phil3}, the contact lines of the droplets are immobilized due to the insufficient residual energy to overcome the resistance. However, on S_{Phob2} and S_{Phob3}, the higher residual energy provides more power to overcome the resistance caused by CAH. As a result, as shown in **Figures 3.5 l** and **p**, similar to S_{Phil2}, the triple-phase line on S_{Phob2} and S_{phob3} is not completely pinned, but the shrinkage takes a significantly longer time. While hydrophobic surfaces offer the advantage of providing more nucleation sites for droplets, the longer relaxation time associated with these surfaces negates this benefit and ultimately leads to a decrease in the condensation performance.

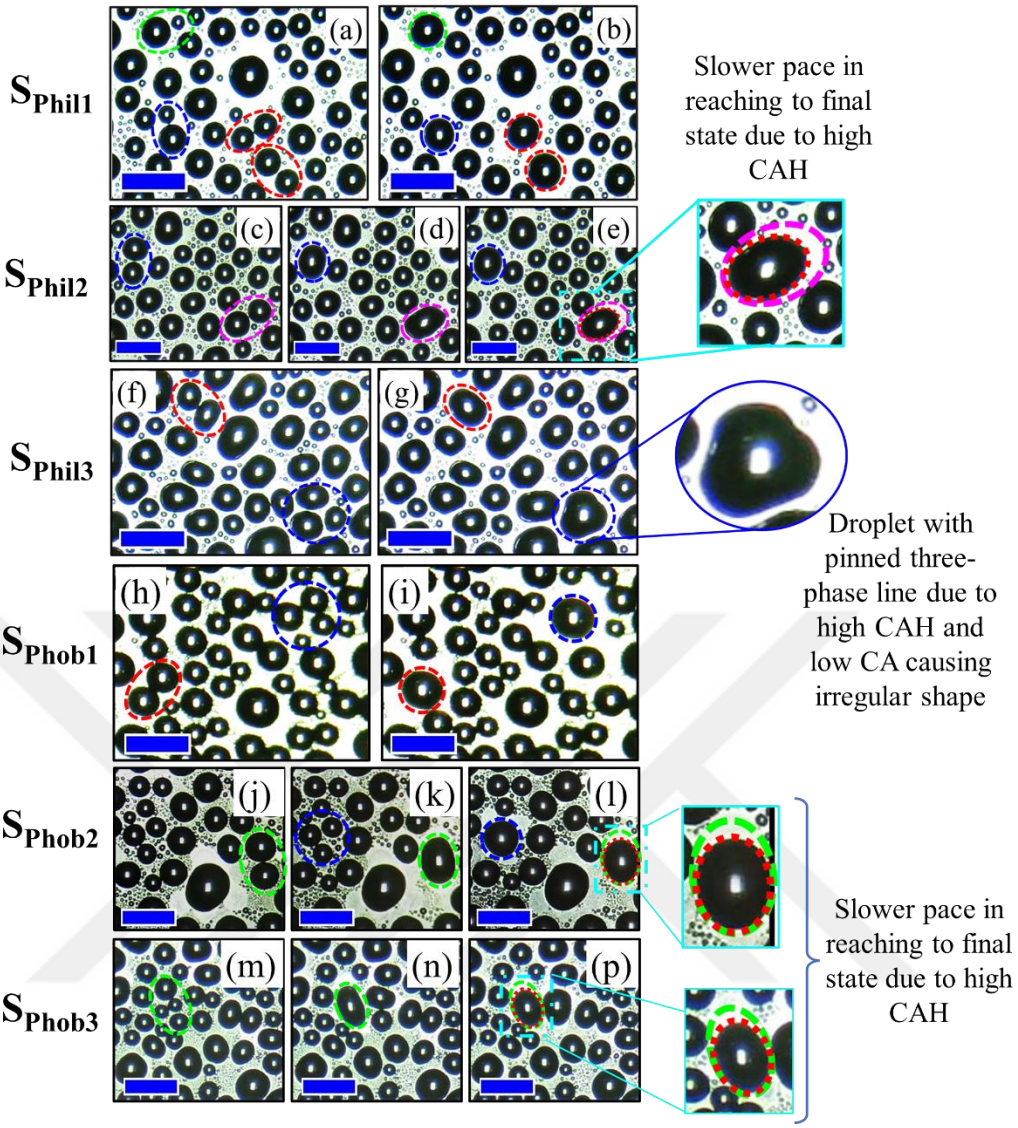

Figure 3.5 Coalescence of droplets on the tested samples. (a and b) S_{Phil1}, (c-e) S_{Phil2}, (f and g) S_{Phil3}, (h and i) S_{Phob1}, (j-l) S_{Phob2}, (m-p) S_{Phob3}

3.1.3 Droplet Distribution

Droplet distribution data were further analyzed and reduced so that the condensation behavior of a surface can be quantitatively analyzed from the droplet density and size distribution and condensate area coverage. Only condensed droplets with a radius greater than 10 μm were considered in this analysis. The radius of the non-circular droplet is approximated using $\sqrt{A_{drop}/\pi}$. All the experiments were conducted at least twice, and the data points presented in this section represent the average values obtained from the experiments.

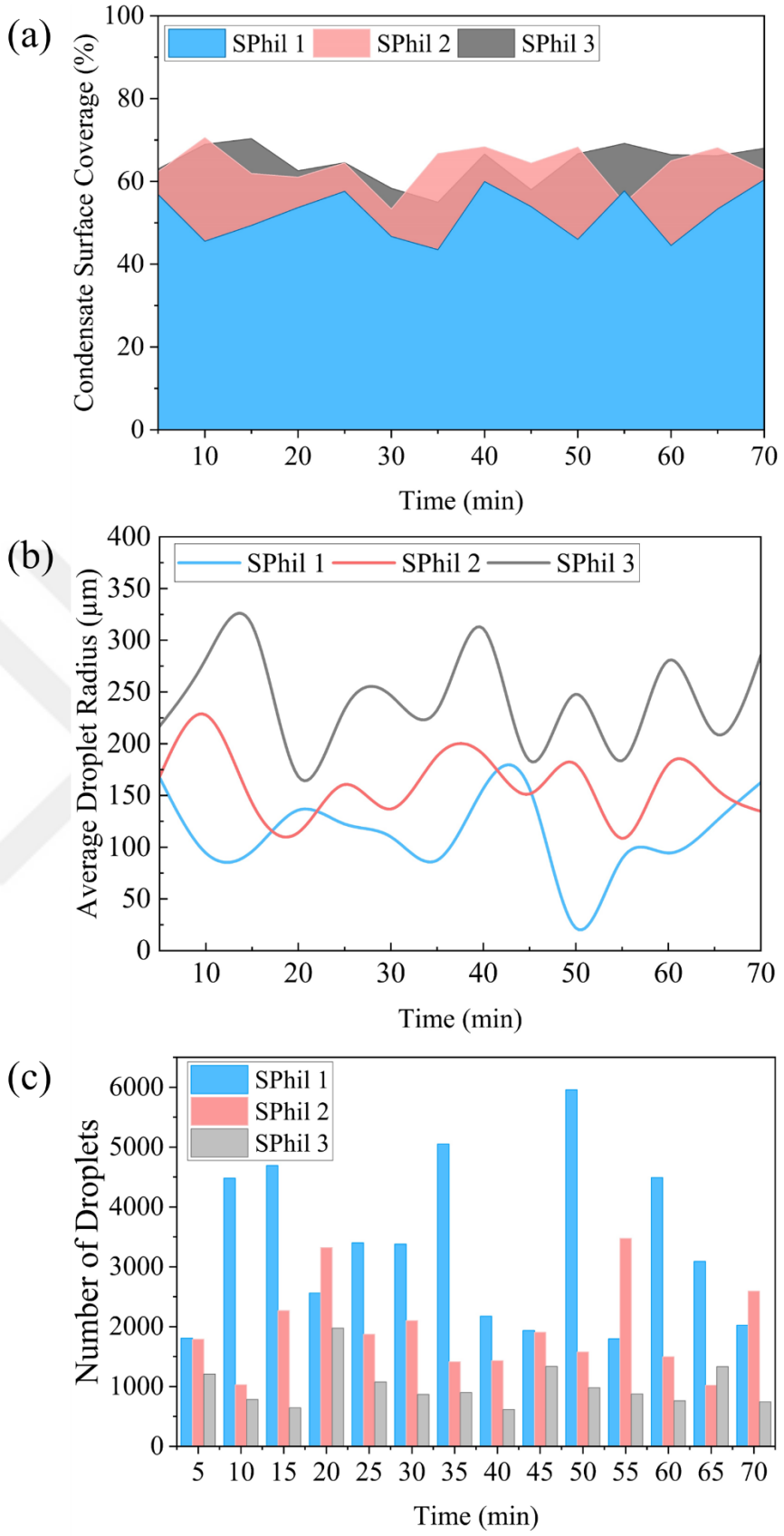

Figure 3.6 (a) Condensate surface coverage, (b) Average radius of droplets, and (c) Number of droplets over time during the experiments for hydrophilic samples.

Figure 3.6 provides results on condensation behavior of hydrophilic surfaces. In **Figure 3.6 a**, the condensate surface coverage is displayed with time. From this figure, it is evident that the percentage of condensate coverage on S_{Phil1} is generally lower compared to the other hydrophilic surfaces, which suggests the presence of more nucleation sites on S_{Phil1}.

In **Figure 3.6 b**, the average droplet radius on different surfaces is presented. Accordingly, the average radius of droplets on S_{Phil1} is smaller than the other surfaces, which can be attributed to two factors. First, the maximum radius of droplets on S_{Phil1} is smaller than that on other hydrophilic surfaces (**Figure 3.4**). This suggests that droplets on S_{Phil1} tend to have a smaller size. Moreover, the lower surface coverage of S_{Phil1} causes a higher nucleation rate and thus a larger number of smaller droplets, which contributes to a smaller average radius. Moreover, although the surface coverages of S_{Phil2} and S_{Phil3} are relatively close to each other, the average droplet radius on S_{Phil3} is larger than that on S_{Phil2} due to the different behavior of droplets after coalescence. On S_{Phil3}, the triple-phase line of the coalesced droplets remains pinned and cannot shrink. Therefore, larger droplets occupy a significant portion on the surface area. The pinned triple-phase line prevents the droplets from further coalescence and reduces the number of smaller droplets. In contrast, on S_{Phil2}, the lower CAH makes the coalesced droplets shrink and causes a smaller size. Thus, more space for droplet nucleation is provided and a larger number of droplets and faster coalescence are evident. As a result, S_{Phil2} has a shorter condensation cycle duration compared to S_{Phil3}. In **Figure 3.6 c**, the number of droplets is displayed with time. As can be seen, the number of droplets on S_{Phil1} is larger compared to the other surfaces. This is consistent with the larger nucleation rate and smaller average droplet size observed on S_{Phil1}. S_{Phil3} has the lowest number of droplet due to the presence of larger coalesced droplets on this surface.

In summary, the data presented in **Figure 3.6** provides valuable insights into the condensation behavior, surface coverage, droplet size dynamics, and number of droplets on different hydrophilic surfaces. The lower coverage and smaller average droplet size on S_{Phil1} suggest a higher tendency for droplet coalescence and growth. These factors contribute to a shorter condensation cycle duration on this surface. Meanwhile, the close surface coverage but larger average droplet size on S_{Phil3} can be attributed to the presence of larger pinned droplets.

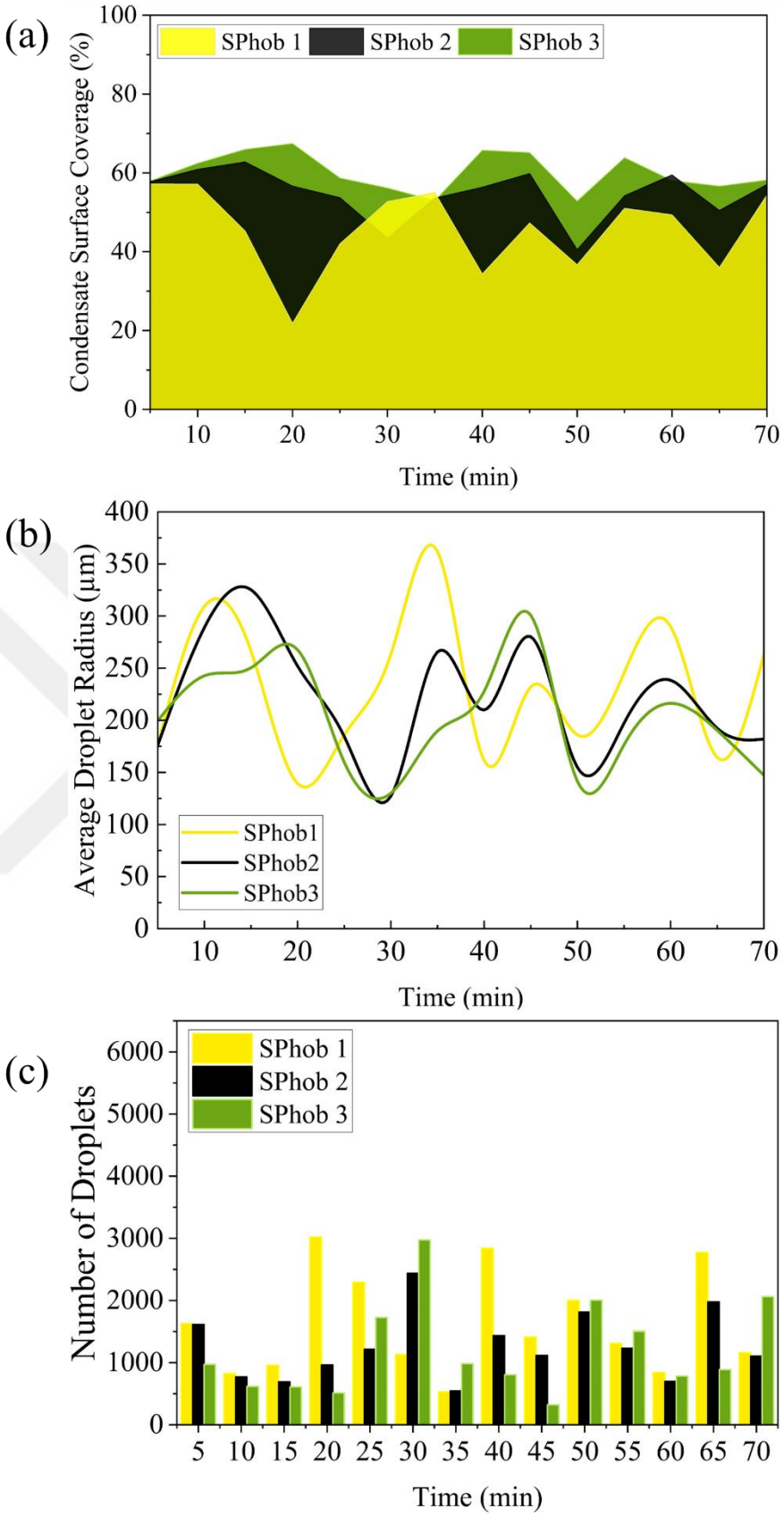

Figure 3.7 (a) Condensate surface coverage, (b) Average radius of droplets, and (c) Number of droplets over time during the experiments for hydrophobic samples

The results of visualization for hydrophobic surfaces are presented in **Figure 3.7**. **Figure 3.7a** shows the condensate coverage on the hydrophobic surfaces. S_{Phob1} has a consistently lower coverage compared to the other hydrophobic surfaces during the experiments (except from t=30min to t=35min). This lower coverage on S_{Phob1} can be attributed to its lower CAH compared to the other surfaces as well as its higher CA compared to S_{Phob3}. The lower coverage on S_{Phob1} is advantageous as it provides more nucleation sites and promotes condensation heat transfer. Among the three hydrophobic surfaces, S_{Phob3} has the largest condensate surface coverage due to its larger maximum droplet radius (r_{max}), lower CA, and high CAH. The lower CA of the surface is linked with higher wettability, which gives rise to more and faster droplet nucleation. Moreover, the smaller contact angle facilitates droplet formation and growth, while higher CAH on S_{Phob3} prevents droplet shrinkage after coalescence, which leads to larger droplets on the surface.

Figure 3.7 b displays the fluctuations in the average droplet size on the hydrophobic. Accordingly, S_{Phob1} has larger fluctuations compared to the other surfaces. This behavior can be linked with a high CA and lower CAH on S_{Phob1}, which enables more frequent and faster droplet coalescence. Thus, new droplets merge into larger droplets, and there exist a decrease in the number of small droplets and an increase in the average droplet size.

During the departure stage of condensation, the removal of larger droplets has a significant effect on the average droplet size (t=20min in **Figure 3.7 b**). The departure of larger droplets generates vacant areas, which are suitable for the nucleation of new droplets. This contributes to the decrease in both the surface coverage and average droplet size of S_{Phob1} while simultaneously raising the number of droplets at the same time.

It should be noted that although the surface coverage of all surfaces is close to each other at t=5min, the number of droplets on S_{Phob3} is lower compared to the other two surfaces. This can be explained with the higher wettability of S_{Phob3}, which leads to faster droplet nucleation and subsequent coalescence. Additionally, due to the surface resistance of S_{Phob3} against the movement of merged droplets' contact line, the droplets after coalescence tend to have larger radii, as evident in **Figure 3.7 b**. At t=5min, the numbers of droplets and their average size on S_{Phob1} and S_{Phob2} are equal, which implies that their condensation cycles are at the initial coalescence stage, and the effect of their difference in CAH is not yet evident.

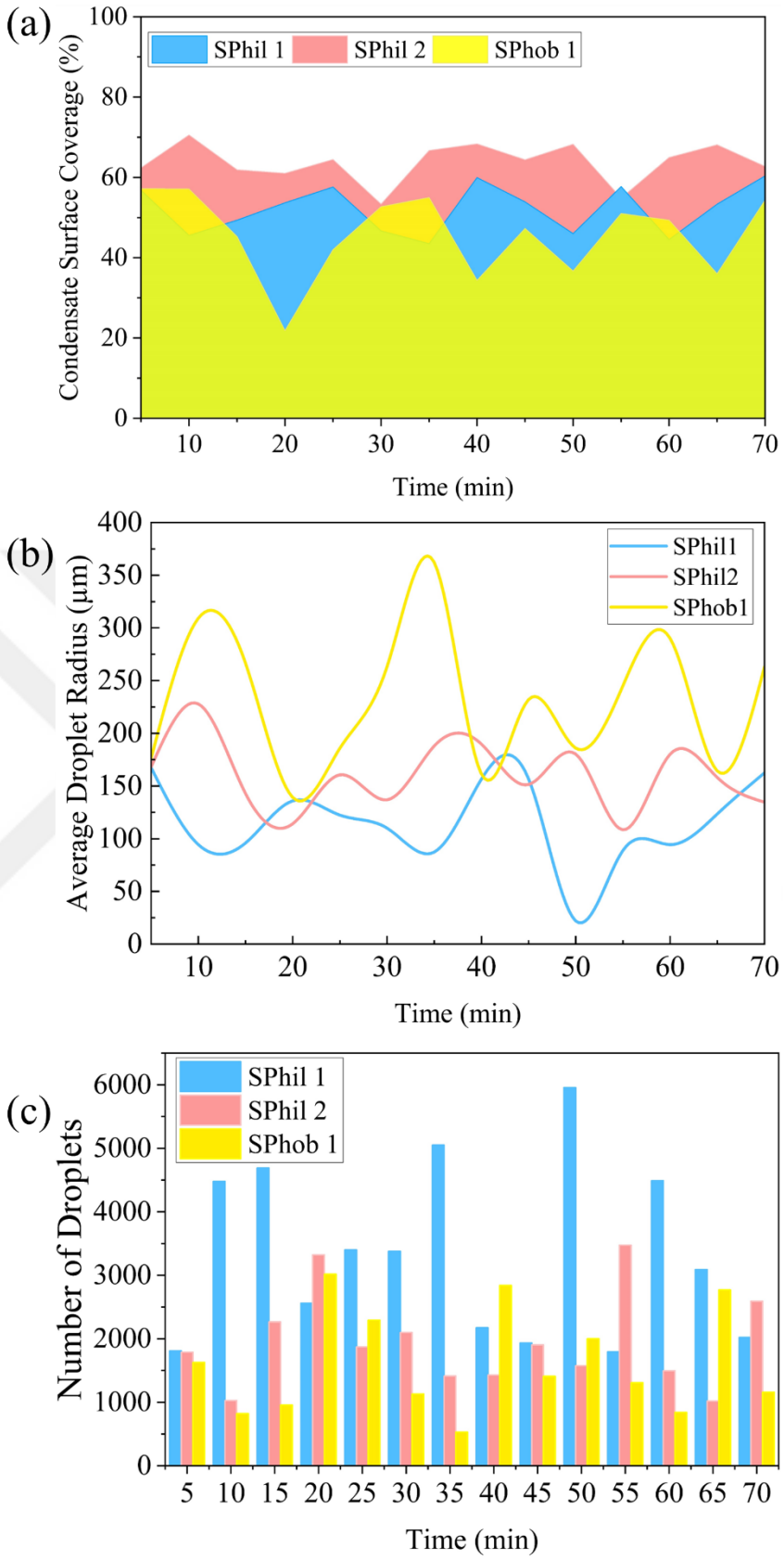

Figure 3.8 (a) Condensate surface coverage, (b) Average radius of droplets, and (c) Number of droplets over time during the experiments for samples with lower CAH.

Figure 3.8 displays the results of image analysis for S_{Phil1}, S_{Phil2}, and S_{Phob1}, which are the three surfaces with lower CAH among the fabricated surfaces. during the experiments, the surface coverage of S_{Phob1} is lower than that of S_{Phil2}, and in most time slots, it is also lower than S_{Phil1}. Moreover, the average droplet radius for S_{Phob1} is larger compared to the other two surfaces. This suggests that S_{Phob1} is mostly covered with larger droplets, and the lack of small droplets contributes to the increased average droplet size. The smaller number of droplets on S_{Phob1} further supports this observation (**Figure 3.8 c**). In contrast, both S_{Phil1} and S_{Phil2} house smaller average droplet sizes due to a higher number of small droplets, which is facilitated by their wetting nature.

It can be seen in **Figure 3.8** that among these three surfaces S_{Phil1} has the best performance. It has the largest number of droplets and also has the smallest average size in most of time slots. Moreover, the combination of high nucleation rate and shorter cycle duration reveal its great removal performance. These two characteristics, better nucleation and better drainage, are the most important factors in condensation heat transfer. Accordingly, a surface which is outstanding in both of them has for sure a better condensation heat transfer performance. However, it is challenging to determine whether S_{Phil2} or S_{Phob1} has a better performance. While S_{Phob1} has a lower surface coverage, which means there are more nucleation sites, S_{Phob2} has a better nucleation rate due to its lower contact angle. Moreover, although S_{Phil2} has a larger maximum droplet radius (r_{max}), which might negate its nucleation rate advantage, its cycle duration is comparable to that of S_{Phob1}.

These findings highlight the influence of surface properties on droplet behavior and coalescence dynamics, which play a vital role in condensation heat transfer and surface design for various applications.

3.2. Heat Transfer

Figure 3.9 illustrates the average condensation heat-transfer coefficients of the examined surfaces at 100% relative humidity, a surface temperature of 2°C, and an ambient temperature of 21.5°C. Among the surfaces, S_{Phil1} has the highest heat-transfer coefficient (HTC), followed by S_{Phob1}, S_{Phil2}, S_{Phob2}, S_{Phil3}, and S_{Phob3}, in descending order (**Figure**

3.10). Comparing these surfaces to the reference surface S_{Phil2}, it can be observed that S_{Phil1} and S_{Phob1} have 20% and 15% higher HTC, respectively, while S_{Phob2}, S_{Phil2}, and S_{Phob3} have 17%, 19%, and 25% lower HTC compared to S_{Phil2}.

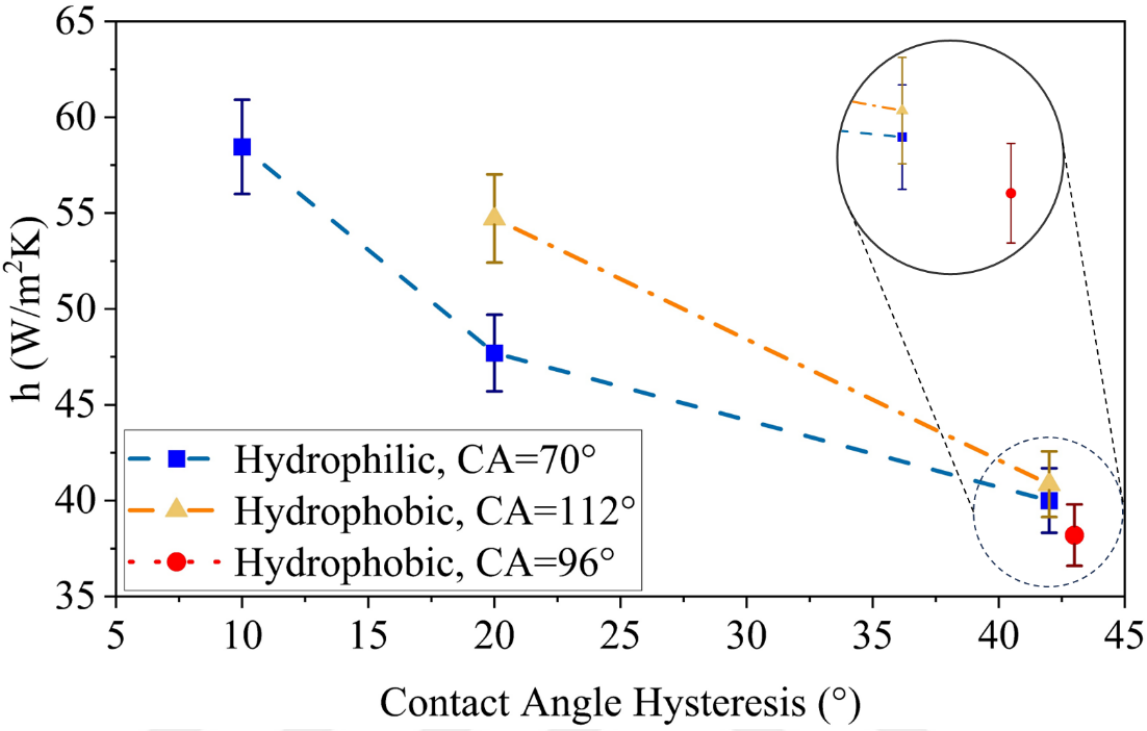

Figure 3.9 Condensation heat transfer coefficient for different CAH values for RH=100%

The static contact angles of S_{Phil1}, S_{Phil2}, and S_{Phil3} are nearly identical, which suggests that the differences in their heat-transfer coefficients are primarily influenced by their varying CAH. Interestingly, although the CAH difference between S_{Phil1} and S_{Phil2} is half of the CAH difference between S_{Phil2} and S_{Phil3}, the difference in the heat-transfer coefficient between S_{Phil1} and S_{Phil2} is slightly greater than the difference between S_{Phil2} and S_{Phil3}. This finding emphasizes on the impact of low hysteresis surfaces on condensation heat transfer.

In the case of hydrophobic surfaces, S_{Phob1} and S_{Phob2} have similar static contact angles but different CAH values. Despite the similarity in contact angles, the differences in heat-transfer coefficients are larger for the hydrophobic surfaces compared to the hydrophilic ones. The increase in CAH on hydrophobic surfaces leads to the presence of larger pinned droplets, which reduces the available nucleation sites and restricts droplet shrinking after

coalescence. Consequently, the benefits of increased nucleation space and easier droplet drainage are counteracted by the higher CAH value.

Furthermore, **Figure 3.9** demonstrates that when the contact angle is held fixed, increasing CAH results in a decrease in the condensation heat transfer performance for both hydrophobic and hydrophilic surfaces. However, this relationship is not valid for surfaces with similar CAH but different contact angles. For instance, S_{Phil3}, S_{Phob2}, and S_{Phob3} have close contact angle hysteresis values but different contact angles. Interestingly, S_{Phob3}, of a larger contact angle than S_{Phil3} but a smaller contact angle than S_{Phob2}, has a smaller heat-transfer coefficient compared to both S_{Phil3} and S_{Phob2}. This can be attributed to the lower wettability of S_{Phob3}, which results in a reduced droplet nucleation rate. However, the departure radius of droplets on S_{Phob3} is close to the r_{max} observed on S_{Phil2} and S_{Phil3}. **Figures 3.6 b** and **3.7 b** indicate that although the condensate surface coverage for S_{Phob3} is close to that of S_{Phil2} and S_{Phil3}, S_{Phil3} outperforms S_{Phob3} in terms of droplet nucleation. Also, S_{Phob2} has a larger heat-transfer coefficient compared to S_{Phob3}. This can be linked to the smaller percentage of condensate surface coverage on S_{Phob2}, which allows more locations for nucleation. Due to the higher contact angle, the maximum radius of droplets on S_{Phob2} is smaller than on S_{Phob3}, which reduces the contact area with the surface and facilitates better and faster droplet removal.

Figure 3.10 presents the heat-transfer coefficient profile for the surfaces at different relative humidity (RH) values. As can be seen, decreasing RH reduces the differences between the heat-transfer coefficients of the surfaces and flattens the overall profile.

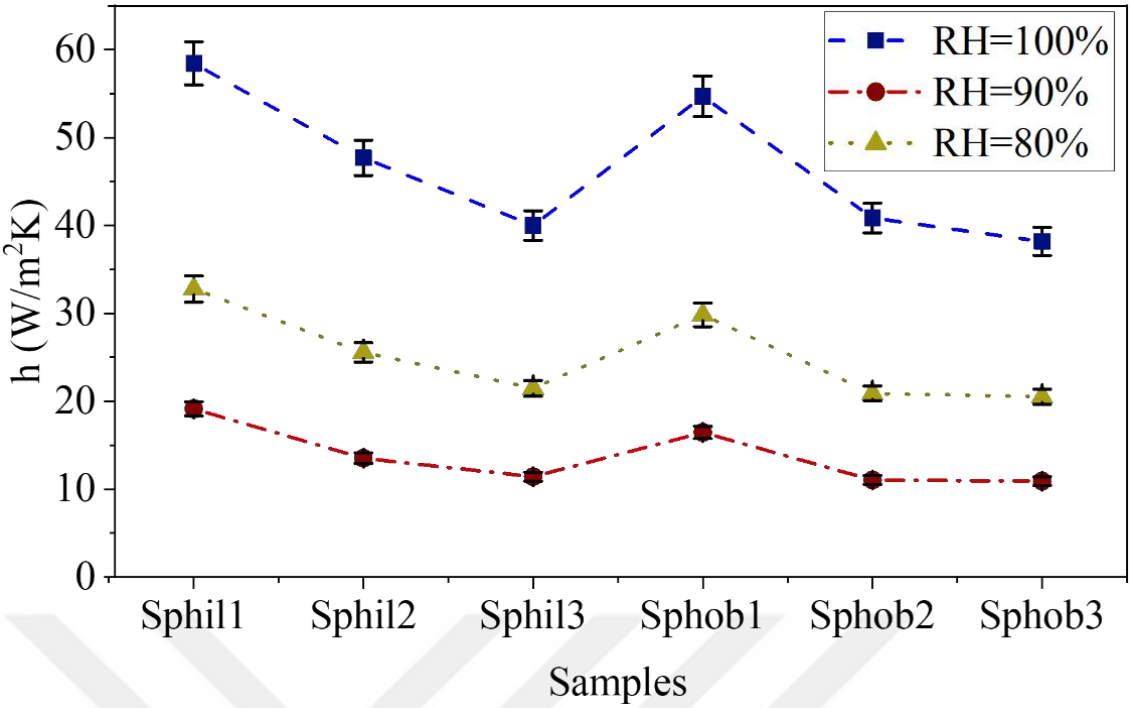

Figure 3.10 Condensation heat transfer coefficient of the samples for different relative humidities

3.3.Condensation Mechanisms and Discussion

3.3.1 Nucleation and Growth

Nucleation is the initial stage of a condensation cycle, as described by Volmer's nucleation theory [39]. This theory states that for liquid droplets to form on a surface, a minimum energy barrier ΔG must be overcome. The energy barrier can be calculated using the following equation:

$$\Delta G = \frac{\pi {r_{min}}^2 \sigma (2 - 3cos\theta + cos^3\theta)}{3} \quad (3.1)$$

where θ and r_{min} correspond to the static contact angle and minimum nucleation radius, respectively. The equation to calculate r_{min} is expressed as:

$$r_{min} = \frac{2\sigma T_{sat}}{\rho_l h_{fg} \Delta T} \quad (3.2)$$

where ρ_l, h_{fg}, and ΔT are the liquid density, latent heat of phase change, and temperature difference between the vapor and condensing surface. The impact of the contact angle on the free energy barrier for condensation is clearly evident.

The equilibrium contact angle, also known as the Young's contact angle, represents the angle formed between the solid surface and the tangent line to the liquid-air interface at the point where the liquid meets the surface (**Figure 2.1 a**), when the system is in thermodynamic equilibrium. The equilibrium contact angle is determined by the balance of intermolecular forces among the solid, liquid, and air phases.

Hydrophilic surfaces exhibit a lower energy barrier, making the nucleation process easier compared to hydrophobic surfaces. When the contact angle is increased from 70° (S_{Phil2}) to 112° (S_{Phob1}) (as in our study), a substantial increase (204%) can be observed in the energy barrier ΔG. This explains why droplet nucleation, growth, and coalescence processes occur more easily and rapidly on hydrophilic surfaces compared to hydrophobic surfaces (see **Figures 3.2** and **3.4**)

Once the droplet nucleates, it begins to cool down. As its surface temperature decreases below the temperature of the surrounding humid air, the vapor in the air begins to condense onto the surface of the droplet. This condensation leads to the growth of the droplet. During the initial stages of droplet formation, when the droplet is in a static state, CAH will not be a contributing factor.

3.3.2 Coalescence

As the density of droplets on the surface increases and they come into contact with each other, they begin to merge and form larger droplets. This process is known as coalescence, which is the third stage of condensation following droplet nucleation and growth through direct condensation (as depicted in **Figures 3.1** and **3.2**). The coalescence of droplets involves interactions between the droplets and surface, and understanding the underlying mechanisms requires discussion about the involved contributing factors.

In **Figure 3.11**, the process of droplet coalescence on a surface is illustrated. During coalescence, the droplet undergoes significant deformations both at the interface and triple-phase line, where various forms of energy and forces are involved [40–43]. In terms of energy, there are multiple factors at play, including surface energy, viscous dissipation,

gravitational potential energy, and energy dissipation on the triple-phase lines. From a force perspective, in addition to surface tension, there are internal viscous forces and gravitational forces. Moreover, the coalescence process involves resistances on receding triple-phase lines (F_{rec}) and the advancing triple-phase lines (F_{adv}) due to the presence of surface contact angle hysteresis. These factors collectively influence the dynamics of droplet coalescence.

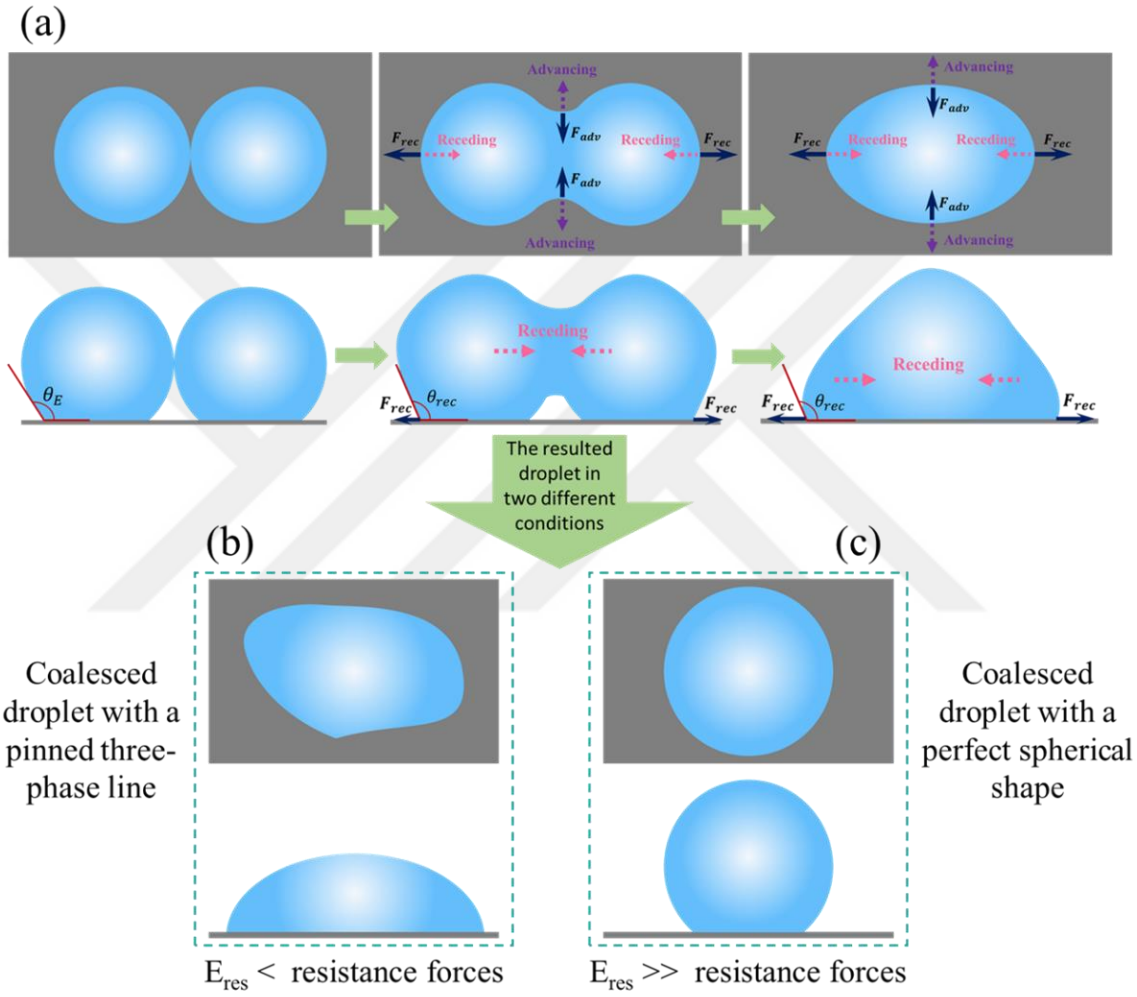

Figure 3.11 Droplet coalescence process. (a) Change in droplet geometry and the resistance forces applied on the three-phase line. (b) The coalesced droplet with a pinned three-phase line indicates that E_{res} was insufficient to overcome the resistance. (c) The coalesced droplet, displaying a perfect spherical shape, demonstrates that E_{res} was sufficiently high to completely overcome the resistance forces.

By neglecting gravity for small droplets, the contact angle plays a significant role in determining the amount of surface energy released (ΔE_{sur}) and the residual energy (E_{res})

remaining after accounting for viscous dissipation (ΔE_{vis}) [41,42,44]. ΔE_{sur} and E_{res} can be defined as follows:

$$\Delta E_{sur} = \sigma_{lg}\Delta A_{lg} + \sigma_{gs}\Delta A_{gs} + \sigma_{sl}\Delta A_{sl} \quad (3.3)$$

$$E_{res} = \Delta E_{sur} - \Delta E_{vis} \quad (3.4)$$

where ΔA is the change in the interfacial area.

When two droplets with equal radii coalesce, an increase in the contact angle leads to an increase in both ΔE_{sur} (released surface energy) and E_{res} (residual energy). This indicates an increase in the driving power for the coalesced droplet. It is worth noting that there exists a threshold value of the contact angle for the coalescence of droplets with specific radii, as reported in the study by Chu et al. [45]. If the static static contact angle is below this threshold, there is no residual energy left, suggesting that the surface energy is not sufficiently small.

Unlike the equilibrium contact angle, which primarily influences the presence of residual energy after coalescence, the contact angle hysteresis plays a significant role in determining the resistances (F_{adv} and F_{rec}) and energy dissipation (ΔE_{cah}) occurring on the droplets contact lines [46–48]. A higher contact angle hysteresis results in increased resistances along the droplet contact line, requiring more E_{res} to overcome the energy dissipation. In summary, while the equilibrium contact angle determines the presence of E_{res} after coalescence, the contact angle hysteresis governs the resistances and energy dissipation on the droplet contact line when the coalesced droplet undergoes shrinking or movement.

On S_{Phil3}, which has low CA but large CAH, the low value of ΔE_{sur} indicates the absence of E_{res} after droplet coalescence, while the high surface resistance to triple-phase line movement is evident. As a consequence, the surface tension alone is insufficient to overcome the resistances on the triple-phase line, leading to the formation of strongly pinned coalesced droplets with irregular shapes (**Figure 3.5 g**). With no residual energy available to facilitate movement, the coalesced droplets remain in a pinned state. The comparison between the results obtained from S_{Phil3} and S_{Phob3} (**Figure 3.5**) highlights the influence of higher ΔE_{sur}, which is attributed to the larger CA on S_{Phob3}. Despite the longer relaxation time observed on S_{Phob3}, the triple-line is not pinned in the same manner as

S_{Phil3}. Interestingly, upon examining the coalescence of two sets of droplets with similar radii on S_{Phob2} and S_{Phob3}, it can be observed that the area of the coalesced droplet on S_{Phob2} decreases by 28% after relaxation, whereas for S_{Phob3}, this decrease is only 20%.

For S_{Phil1}, which has a low contact angle and low contact angle hysteresis, the dynamics is distinct. Although the E_{res} left after droplet coalescence is low, the resistance on the droplet contact line is also minimal. As a result, the resulted droplet after coalescence maintains a circular cross section (**Figures 3.5 a and b**). While these droplets are unable to move spontaneously, they can be easily influenced by external forces such as wind or gravity.

In the case of S_{Phob3}, which has both a large static contact angle and a large contact angle hysteresis, the E_{res}, which is needed to counteract the energy dissipation on the droplet contact line, becomes a critical. As the triple-phase line gradually shrinks, the remaining energy is gradually decreases, which makes the coalesced droplet remain in a pinned state (**Figures 3.5 m-p**).

Surfaces with a large contact angle and low contact angle hysteresis offer suitable conditions for self-propelled droplet motion. When the contact angle (CA) is increased to a sufficient level, it can even lead to droplet jumping [18,49]. In these cases, the coalesced droplet retains sufficient residual energy, while the energy dissipation on the triple-phase line is minimal. As a result, the coalescence process occurs rapidly on surfaces such as S_{Phob1}, and the resulting droplets maintain a perfect spherical shape.

These distinct behaviors highlight the importance of both contact angle and contact angle hysteresis in determining the mobility and shape of coalesced droplets. The interplay between these factors provides insights into the dynamics of droplet coalescence and subsequent movement of coalesced droplets on different surfaces.

3.3.3 Departure

The final stage of the condensation cycle is the droplet departure. In flow condensation, droplets are removed from the surface due to the vapor shear stress force acting on the droplet interface. This means that even droplets that have not reached their maximum radius might be removed from the surface due to the flow-droplet shear force in the flow

direction. On tilted or vertically oriented surfaces without external forces, droplet removal is determined by the opposing forces of gravity (downward) and droplet contact area adhesion (in the opposite direction). To detach a droplet from the surface, the force of gravity must surpass the adhesion force. As the droplets grow, they merge with nearby droplets and continue to expand until they reach the departure radius. At this point, their mass becomes large enough to overcome the adhesion force. Antonini et al. [50] determined the quantified adhesion force acting on a liquid droplet, independent of its shape, as follows:

$$F_{adh} = -\sigma \int_0^L cos\theta(l) cos\psi(l) \tag{3.5}$$

where L represents the length of the contact line. The calculation of the distributions $\theta(l)$ (the distributions of the contact angle) and $\Psi(l)$ (the distribution of the normal along the contact line) along the contact line can be challenging due to the irregular shape of the droplets. However, Amirfazli et al. [51] introduced a parameter k to address this complexity. The parameter k takes into account the contact angle distribution and considers irregular and deformed shapes of the liquid droplet. Consequently, Equation 6 can be simplified using this parameter as follows:

$$F_{adh} = k\sigma(cos\theta_{min} - cos\theta_{max})L_b \tag{3.6}$$

The expression ($\cos\theta_{min} - \cos\theta_{max}$) denotes the contact angle hysteresis, and L_b represents the length of the drop base. In the case where we assume the droplet to have a hemispherical shape, the length of the drop base is equivalent to the droplet's diameter, $L_b = D$.

Equation 7 highlights the significance of CAH in droplet removal, as it directly affects the adhesion force. Furthermore, CAH also influences the length of the contact line. The interplay between CAH and CA becomes crucial during droplet coalescence, where surface properties determine whether the droplets shrink, reducing their contact line length, or its border become pinned to the surface, resulting in a larger contact line. While both CAH and CA impact the adhesion force, the role of CAH is more prominent in this regard. In a study conducted by Becher-Nienhaus et al. [52] on micropatterned checkboard-like surfaces, two types of micropatterned bi-philic surfaces were fabricated, each with different pattern sizes. One type of surface had matching contact angle hysteresis (CAH) regions, while the other type had regions with mismatched CAH. The

findings of their study revealed an interesting result regarding the dominant influence of CAH on dynamic wettability. Specifically, they observed that the dynamic wettability remained consistent in samples with matching regional CAH, regardless of the presence of hydrophilic regions or variations in pattern size. This highlights the significant role of CAH in controlling droplet behavior and removal on such micropatterned surfaces.

The droplets need to reach a mass at which the force of gravity overcomes the adhesion so that the droplets could be swiped from the surface:

$$mg = k\sigma(cos\theta_{min} - cos\theta_{max})L_b \tag{3.7}$$

For the hydrophilic surfaces in our experiments the adhesion force on S_{Phil3} is 115% higher than S_{Phil2}, and the adhesion force on S_{Phil2} is 141% higher than S_{Phil1}. Although the CAH difference between S_{Phil1} and S_{Phil2} is 10 degrees, the difference in maximum radius causes a large difference in the adhesion force. Moreover, the adhesion force on S_{Phob2} is 145% higher than S_{Phob1} which is 30% higher than the difference between S_{Phil3} and S_{Phil2}. This notable difference highlights that increasing CAH on hydrophobic surfaces has a more negative impact.

4. CONCLUSION

In this study, our aim was to investigate how changes in contact angle (CA) and contact angle hysteresis (CAH) influence condensation heat transfer. For this, we fabricated a set of surfaces with varying CA and CAH values and conducted experiments to analyze the impact on droplet dynamics and condensation performance. By understanding these effects, we can gain insights into optimization of condensation heat transfer for various applications.

Our findings revealed that increasing CAH while keeping CA constant had a consistent negative effect on condensation heat transfer. However, the relationship between CA and condensation performance was not linear, indicating the complex nature of these interactions. We observed that changes in CAH had a greater influence on the condensation performance at lower CAH values compared to higher values, which highlightes the importance of considering the entire range of CAH values.

Furthermore, our study demonstrated that the effects of CAH were more pronounced on hydrophobic surfaces compared to hydrophilic surfaces. The reduction in CAH on hydrophilic surfaces resulted in a greater enhancement on condensation heat transfer compared to increasing CA. These results emphasize the significant role of CAH in the efficiency of heat transfer during condensation.

The observed impact of CAH on condensation heat transfer can be attributed to its influence on droplet coalescence and removal. Increasing CAH led to larger droplet sizes and longer condensation cycle durations, which causes increased resistance to droplet movement and drainage. These findings highlight the importance of considering both CA and CAH when designing surfaces for optimum condensation heat transfer.

In summary, our investigation provides valuable insights into the role of static and dynamic contact angles in condensation heat transfer. These findings can guide the design and serve in the optimization of surfaces for enhanced heat transfer in condensation-based applications. Further research in this field will help advance our understanding and facilitate the development of innovative approaches for efficient condensation heat transfer in various industries.

4.1. Future research directions

Suggested future research offers can be listed as:

• In this thesis, contact angles ranging from 70 to 110 and hysteresis values from 10 to 40 were investigated. Expanding the investigation range would provide deeper insights into the impact of CA and CAH on condensation performance. Additionally, the study examined three relative humidities as condensation conditions. More parameters could be considered such as different subcooling temperatures and surface orientations, to simulate real-world applications such as solar-driven water desalination systems with inclined downward surfaces for vapor condensation.

• Enhancing the durability of low hysteresis hydrophilic surfaces and developing fabrication techniques for achieving low hysteresis on metallic substrates to be used in industrial applications are crucial aspects to address.

• In this thesis, humid air condensation experiments were conducted to compare the impact of static and dynamic contact angles on condensation performance. Flow condensation experiments could be conducted in different flow rates as well as different steam qualities to gain further insights into the effect of static and dynamic contact angles.

4.2. Contribution to the literature

While contact angle hysteresis (CAH) has been recognized as significant in condensa tion heat transfer performance, no study has provided insights into the comparison between

CA and CAH for surface design optimization. This thesis compares the impact of static and dynamic contact angles and has the following contributions to the fields:

• This thesis showed that condensation heat transfer can be improved not only by increasing contact angle to achieve dropwise condensation but also by decreasing contact angle hysteresis, which can have a stronger impact.

• This thesis revealed that changes in contact angle hysteresis had a greater influence on condensation performance at lower Contact angle hysteresis values compared to higher values. Moreover, the negative impact of increasing contact angle hysteresis is more pronounced on hydrophobic surfaces compared to hydrophilic surfaces due to the decrease in nucleation sites.

• This thesis demonstrated that Increasing contact angle hysteresis while keeping contact angle constant consistently negatively affected condensation heat transfer. However, the impact of increasing contact angle in constant contact angle hysteresis can be either positive or negative, depending on the Contact angle hysteresis value and the amount of change in contact angle.

BIBLIOGRAPHY

[1] A. Nagar, T. Pradeep, Clean Water through Nanotechnology: Needs, Gaps, and Fulfillment, 23 (2022) 54. https://doi.org/10.1021/acsnano.9b01730.

[2] D. Seo, J. Lee, C. Lee, Y. Nam, The effects of surface wettability on the fog and dew moisture harvesting performance on tubular surfaces OPEN, (2016). https://doi.org/10.1038/srep24276.

[3] N. Lukic, L.L. Diezel, A.P. Fröba, A. Leipertz, Economical aspects of the improvement of a mechanical vapour compression desalination plant by dropwise condensation, Desalination. 264 (2010) 173–178. https://doi.org/10.1016/J.DESAL.2010.07.023.

[4] C. Du, C. Huang, A floating vapor condensation structure in a heat-localized solar evaporation system for facile solar desalination, Appl Therm Eng. 201 (2022) 117834. https://doi.org/10.1016/J.APPLTHERMALENG.2021.117834.

[5] Z. Rao, S. Wang, M. Wu, Z. Lin, F. Li, Experimental investigation on thermal management of electric vehicle battery with heat pipe, Energy Convers Manag. 65 (2013) 92–97. https://doi.org/10.1016/J.ENCONMAN.2012.08.014.

[6] I. Mudawar, Assessment of high-heat-flux thermal management schemes, IEEE Transactions on Components and Packaging Technologies. 24 (2001) 122–141. https://doi.org/10.1109/6144.926375.

[7] J. Bao, Y. Lin, R. Zhang, N. Zhang, G. He, Strengthening power generation efficiency utilizing liquefied natural gas cold energy by a novel two-stage condensation Rankine cycle (TCRC) system, Energy Convers Manag. 143 (2017) 312–325. https://doi.org/10.1016/J.ENCONMAN.2017.04.018.

[8] S. Wang, X. Yu, C. Liang, Y. Zhang, Enhanced condensation heat transfer in air-conditioner heat exchanger using superhydrophobic foils, Appl Therm Eng. 137 (2018) 758–766. https://doi.org/10.1016/J.APPLTHERMALENG.2018.04.020.

[9] B. El Fil, G. Kini, S. Garimella, A review of dropwise condensation: Theory, modeling, experiments, and applications, Int J Heat Mass Transf. 160 (2020) 120172. https://doi.org/10.1016/j.ijheatmasstransfer.2020.120172.

[10] J.W. Rose, Condensation Heat Transfer Fundamentals, Chemical Engineering Research and Design. 76 (1998) 143–152. https://doi.org/10.1205/026387698524712.

[11] J.W. Rose, Dropwise condensation theory and experiment: A review, Http://Dx.Doi.Org/10.1243/09576500260049034. 216 (2002) 115–128. https://doi.org/10.1243/09576500260049034.

[12] M. Alwazzan, K. Egab, B. Peng, J. Khan, C. Li, Condensation on hybrid-patterned copper tubes (I): Characterization of condensation heat transfer, Int J Heat Mass Transf. 112 (2017) 991–1004. https://doi.org/10.1016/J.IJHEATMASSTRANSFER.2017.05.039.

[13] K.S.-A. of the N.Y.A. of Sciences, undefined 1920, Contributions to the herpetology of Porto Rico, Library.Iucn-Isg.Org. (n.d.). http://library.iucn-isg.org/documents/1920/Schmidt_1920_Annals_of_the_New_York_Academy_of_Sciences.pdf (accessed June 25, 2022).

[14] X. Hu, Q. Yi, X. Kong, J. Wang, A review of research on dropwise condensation heat transfer, Applied Sciences (Switzerland). 11 (2021) 1–18. https://doi.org/10.3390/app11041553.

[15] L. Liu, S. Wang, X. Zeng, P. Pi, X. Wen, Dropwise Condensation by Nanoengineered Surfaces: Design, Mechanism, and Enhancing Strategies, Adv Mater Interfaces. 8 (2021) 1–19. https://doi.org/10.1002/admi.202101603.

[16] A. Goswami, S.C. Pillai, G. McGranaghan, Surface modifications to enhance dropwise condensation, Surfaces and Interfaces. 25 (2021) 101143. https://doi.org/10.1016/j.surfin.2021.101143.

[17] M.M. Chehrghani, T. Abbasiasl, A.K. Sadaghiani, A. Koşar, Copper-Based Superhydrophobic Nanostructures for Heat Transfer in Flow Condensation, ACS Appl Nano Mater. 4 (2021) 1719–1732. https://doi.org/10.1021/acsanm.0c03181.

[18] T.M. Thomas, P. Sinha Mahapatra, Condensation of Humid Air on Superhydrophobic Surfaces: Effect of Nanocoatings on a Hierarchical Interface, Langmuir. 37 (2021) 12767–12780. https://doi.org/10.1021/ACS.LANGMUIR.1C01012/ASSET/IMAGES/LARGE/LA1C01012_0010.JPEG.

[19] N. Miljkovic, R. Enright, Y. Nam, K. Lopez, N. Dou, J. Sack, E.N. Wang, Jumping-droplet-enhanced condensation on scalable superhydrophobic nanostructured surfaces, Nano Lett. 13 (2013) 179–187. https://doi.org/10.1021/NL303835D/SUPPL_FILE/NL303835D_SI_006.AVI.

[20] J.B. Boreyko, C.H. Chen, Self-propelled dropwise condensate on superhydrophobic surfaces, Phys Rev Lett. 103 (2009) 184501. https://doi.org/10.1103/PHYSREVLETT.103.184501/FIGURES/5/MEDIUM.

[21] K.K. Varanasi, M. Hsu, N. Bhate, W. Yang, T. Deng, Spatial control in the heterogeneous nucleation of water, Appl Phys Lett. 95 (2009) 94101. https://doi.org/10.1063/1.3200951/338532.

[22] M.M. Chehrghani, T. Abbasiasl, A.K. Sadaghiani, A. Koşar, Biphilic Surfaces with Optimum Hydrophobic Islands on a Superhydrophobic Background for Dropwise Flow Condensation, Langmuir. 37 (2021) 13567–13575. https://doi.org/10.1021/acs.langmuir.1c01844.

[23] T. Abbasiasl, M.M. Chehrghani, A.K. Sadaghiani, A. Koşar, Gradient mixed wettability surfaces for enhancing heat transfer in dropwise flow condensation, Int J Heat Mass Transf. 179 (2021). https://doi.org/10.1016/j.ijheatmasstransfer.2021.121664.

[24] H. Zhao, D. Beysens, From Droplet Growth to Film Growth on a Heterogeneous Surface: Condensation Associated with a Wettability Gradient, Langmuir. 11 (1995) 627–634. https://doi.org/10.1021/la00002a045.

[25] S. Daniel, M.K. Chaudhury, J.C. Chen, Fast Drop Movements Resulting from the Phase Change on a Gradient Surface, Science (1979). 291 (2001) 633–636. https://doi.org/10.1126/SCIENCE.291.5504.633.

[26] J.L. Oestreich, C.W.M. van der Geld, J.L.G. Oliveira, A.K. da Silva, Experimental condensation study of vertical superhydrophobic surfaces assisted by hydrophilic constructal-like patterns, International Journal of Thermal Sciences. 135 (2019) 319–330. https://doi.org/10.1016/J.IJTHERMALSCI.2018.09.024.

[27] D. Orejon, A. Askounis, Y. Takata, D. Attinger, Dropwise Condensation on Multiscale Bioinspired Metallic Surfaces with Nanofeatures, ACS Appl Mater Interfaces. 11 (2019) 24735–24750. https://doi.org/10.1021/acsami.9b06001.

[28] S.F. Zheng, U. Gross, X.D. Wang, Dropwise condensation: From fundamentals of wetting, nucleation, and droplet mobility to performance improvement by advanced functional surfaces, Adv Colloid Interface Sci. 295 (2021) 102503. https://doi.org/10.1016/j.cis.2021.102503.

[29] H.J. Butt, J. Liu, K. Koynov, B. Straub, C. Hinduja, I. Roismann, R. Berger, X. Li, D. Vollmer, W. Steffen, M. Kappl, Contact angle hysteresis, Curr Opin Colloid Interface Sci. 59 (2022) 101574. https://doi.org/10.1016/j.cocis.2022.101574.

[30] H. Barrio-Zhang, É. Ruiz-Gutiérrez, S. Armstrong, G. McHale, G.G. Wells, R. Ledesma-Aguilar, Contact-Angle Hysteresis and Contact-Line Friction on Slippery Liquid-like Surfaces, Langmuir. 36 (2020) 15094–15101. https://doi.org/10.1021/ACS.LANGMUIR.0C02668/ASSET/IMAGES/LARGE/LA0C02668_0006.JPEG.

[31] B.K. Cheng, B. Naccarato, K.J. Kim, A. Kumar, Theoretical consideration of contact angle hysteresis using surface-energy-minimization methods, Int J Heat Mass Transf. 102 (2016) 154–161. https://doi.org/10.1016/J.IJHEATMASSTRANSFER.2016.06.014.

[32] H. Cha, H. Vahabi, A. Wu, S. Chavan, M.K. Kim, S. Sett, S.A. Bosch, W. Wang, A.K. Kota, N. Miljkovic, Dropwise condensation on solid hydrophilic surfaces, Sci Adv. 6 (2020). https://doi.org/10.1126/sciadv.aax0746.

[33] Y. Shin, S. Jeong, K.Y. Lee, S. Woo, W. Hwang, Condensation Heat Transfer Correlation for Micro/Nanostructure Properties of Surfaces, ACS Omega. 7 (2022) 33837–33844. https://doi.org/10.1021/ACSOMEGA.2C02557/ASSET/IMAGES/LARGE/AO2C02557_0006.JPEG.

[34] A. Abbas, G.G. Wells, G. McHale, K. Sefiane, D. Orejon, Silicone Oil-Grafted Low-Hysteresis Water-Repellent Surfaces, ACS Appl Mater Interfaces. 15 (2023) 11281–11295. https://doi.org/10.1021/acsami.2c20718.

[35] M.H. Rausch, A.P. Fröba, A. Leipertz, Dropwise condensation heat transfer on ion implanted aluminum surfaces, Int J Heat Mass Transf. 51 (2008) 1061–1070. https://doi.org/10.1016/J.IJHEATMASSTRANSFER.2006.05.047.

[36] A. Ghosh, S. Beaini, B.J. Zhang, R. Ganguly, C.M. Megaridis, Enhancing dropwise condensation through bioinspired wettability patterning, Langmuir. 30 (2014) 13103–13115. https://doi.org/10.1021/la5028866.

[37] H.W. Coleman, W.G. Steele, Experimentation, validation, and uncertainty analysis for engineers: Fourth edition, Experimentation, Validation, and Uncertainty Analysis for Engineers: Fourth Edition. (2018) 1–368. https://doi.org/10.1002/9781119417989.

[38] X. Jing, Z. Guo, Durable Lubricant-Impregnated Surfaces for Water Collection under Extremely Severe Working Conditions, ACS Appl Mater Interfaces. 11 (2019) 35949–35958. https://doi.org/10.1021/ACSAMI.9B08885/ASSET/IMAGES/LARGE/AM9B08885_0007.JPEG.

[39] M. Volmer, A. Weber, Keimbildung in übersättigten Gebilden, Zeitschrift Für Physikalische Chemie. 119U (1926) 277–301. https://doi.org/10.1515/ZPCH-1926-11927.

[40] H. Vahabi, W. Wang, S. Davies, J.M. Mabry, A.K. Kota, Coalescence-Induced Self-Propulsion of Droplets on Superomniphobic Surfaces, ACS Appl Mater Interfaces. 9 (2017) 29328–29336. https://doi.org/10.1021/ACSAMI.7B09344/ASSET/IMAGES/LARGE/AM-2017-093449_0005.JPEG.

[41] Y. Nam, H. Kim, S. Shin, Energy and hydrodynamic analyses of coalescence-induced jumping droplets, Appl Phys Lett. 103 (2013) 161601. https://doi.org/10.1063/1.4825273/25814.

[42] X. Liu, P. Cheng, 3D multiphase lattice Boltzmann simulations for morphological effects on self-propelled jumping of droplets on textured superhydrophobic surfaces, International Communications in Heat and Mass Transfer. 64 (2015) 7–13. https://doi.org/10.1016/J.ICHEATMASSTRANSFER.2015.03.002.

[43] Y. Nam, D. Seo, C. Lee, S. Shin, Droplet coalescence on water repellant surfaces, Soft Matter. 11 (2014) 154–160. https://doi.org/10.1039/C4SM01647E.

[44] X. Liu, P. Cheng, X. Quan, Lattice Boltzmann simulations for self-propelled jumping of droplets after coalescence on a superhydrophobic surface, Int J Heat Mass Transf. 73 (2014) 195–200. https://doi.org/10.1016/J.IJHEATMASSTRANSFER.2014.01.060.

[45] F. Chu, X. Wu, Y. Zhu, Z. Yuan, Relationship between condensed droplet coalescence and surface wettability, Int J Heat Mass Transf. 111 (2017) 836–841. https://doi.org/10.1016/j.ijheatmasstransfer.2017.04.052.

[46] B. Peng, S. Wang, Z. Lan, W. Xu, R. Wen, X. Ma, Analysis of droplet jumping phenomenon with lattice Boltzmann simulation of droplet coalescence, Appl Phys Lett. 102 (2013) 151601. https://doi.org/10.1063/1.4799650/125858.

[47] Y. Nam, D. Seo, C. Lee, S. Shin, Droplet coalescence on water repellant surfaces, Soft Matter. 11 (2014) 154–160. https://doi.org/10.1039/C4SM01647E.

[48] Y. Cheng, J. Xu, Y. Sui, Numerical investigation of coalescence-induced droplet jumping on superhydrophobic surfaces for efficient dropwise condensation heat transfer, Int J Heat Mass Transf. 95 (2016) 506–516. https://doi.org/10.1016/J.IJHEATMASSTRANSFER.2015.11.074.

[49] Y.L. Wu, J.W. Zheng, M. Muneeshwaran, K.S. Yang, C.C. Wang, Moist air condensation heat transfer enhancement via superhydrophobicity, Int J Heat Mass Transf. 182 (2022) 121973. https://doi.org/10.1016/j.ijheatmasstransfer.2021.121973.

[50] C. Antonim, F.J. Carmona, E. Pierce, M. Marengo, A. Amirfazli, General methodology for evaluating the adhesion force of drops and bubbles on solid surfaces, Langmuir. 25 (2009) 6143–6154. https://doi.org/10.1021/LA804099Z/ASSET/IMAGES/LARGE/LA-2008-04099Z_0012.JPEG.

[51] A.J.B. Milne, A. Amirfazli, Drop shedding by shear flow for hydrophilic to superhydrophobic surfaces, Langmuir. 25 (2009) 14155–14164. https://doi.org/10.1021/LA901737Y/ASSET/IMAGES/LARGE/LA-2009-01737Y_0011.JPEG.

[52] B. Becher-Nienhaus, G. Liu, R.J. Archer, A. Hozumi, Surprising Lack of Influence on Water Droplet Motion by Hydrophilic Microdomains on Checkerboard-like Surfaces with Matched Contact Angle Hysteresis, Langmuir. 36 (2020) 7835–7843. https://doi.org/10.1021/acs.langmuir.0c00808.